Systems/Circuits

High-Fidelity Reproduction of Visual Signals by Electrical Stimulation in the Central Primate Retina

Alex R. Gogliettino,[1,2] Sasidhar S. Madugula,[1,2,3] Lauren E. Grosberg,[2,4] Ramandeep S. Vilkhu,[2,5] Jeff Brown,[2,4,5] Huy Nguyen,[2] Alexandra Kling,[2,4] Paweł Hottowy,[6] Władysław Dąbrowski,[6] Alexander Sher,[7] Alan M. Litke,[7] and E. J. Chichilnisky[2,4,5,8]

[1]Neurosciences PhD Program, Stanford University, Stanford, California 94305, [2]Hansen Experimental Physics Laboratory, Stanford University, Stanford, California 94305, [3]Stanford School of Medicine, Stanford University, Stanford, California 94305, [4]Department of Neurosurgery, Stanford University, Stanford, California 94305, [5]Department of Electrical Engineering, Stanford University, Stanford, California 94305, [6]Faculty of Physics and Applied Computer Science, AGH University of Science and Technology, 30-059, Kraków, Poland, [7]Santa Cruz Institute for Particle Physics, University of California, Santa Cruz, Santa Cruz, California 95064, and [8]Department of Ophthalmology, Stanford University, Stanford, California 94305

Electrical stimulation of retinal ganglion cells (RGCs) with electronic implants provides rudimentary artificial vision to people blinded by retinal degeneration. However, current devices stimulate indiscriminately and therefore cannot reproduce the intricate neural code of the retina. Recent work has demonstrated more precise activation of RGCs using focal electrical stimulation with multielectrode arrays in the peripheral macaque retina, but it is unclear how effective this can be in the central retina, which is required for high-resolution vision. This work probes the neural code and effectiveness of focal epiretinal stimulation in the central macaque retina, using large-scale electrical recording and stimulation *ex vivo*. The functional organization, light response properties, and electrical properties of the major RGC types in the central retina were mostly similar to the peripheral retina, with some notable differences in density, kinetics, linearity, spiking statistics, and correlations. The major RGC types could be distinguished by their intrinsic electrical properties. Electrical stimulation targeting parasol cells revealed similar activation thresholds and reduced axon bundle activation in the central retina, but lower stimulation selectivity. Quantitative evaluation of the potential for image reconstruction from electrically evoked parasol cell signals revealed higher overall expected image quality in the central retina. An exploration of inadvertent midget cell activation suggested that it could contribute high spatial frequency noise to the visual signal carried by parasol cells. These results support the possibility of reproducing high-acuity visual signals in the central retina with an epiretinal implant.

Key words: retina; ganglion cell; implant; electrical stimulation; prosthesis; epiretinal; primate

---

Significance Statement

Artificial restoration of vision with retinal implants is a major treatment for blindness. However, present-day implants do not provide high-resolution visual perception, in part because they do not reproduce the natural neural code of the retina. Here, we demonstrate the level of visual signal reproduction that is possible with a future implant by examining how accurately responses to electrical stimulation of parasol retinal ganglion cells can convey visual signals. Although the precision of electrical stimulation in the central retina was diminished relative to the peripheral retina, the quality of expected visual signal reconstruction in parasol cells was greater. These findings suggest that visual signals could be restored with high fidelity in the central retina using a future retinal implant.

Introduction

Electronic neural implants have the potential to translate our evolving scientific understanding of the nervous system into clinical restoration of sensory and motor functions. An important example is epiretinal implants, which electrically activate retinal ganglion cells (RGCs), causing them to send artificial visual signals to the brain. Although this technology is already a primary treatment for blindness resulting from severe photoreceptor degeneration (Weiland et al., 2011, 2016; Goetz and Palanker, 2016), present-day devices provide limited restoration of vision. One likely reason for this is that all currently available implants activate RGCs of different types simultaneously and indiscriminately, creating artificial neural signals that do not mimic the temporally precise and cell type-specific neural code of the retina (Roska and Meister, 2013). A salient example is the simultaneous activation of ON and OFF cells at the same location, which likely sends conflicting visual information to the brain.

A potential solution would be to develop a high-resolution implant that can precisely reproduce neural activity in the diverse RGC types, which are interspersed on the surface of the retina. Previous *ex vivo* work in the peripheral primate retina has shown that epiretinal electrical stimulation with high-density multielectrode arrays can activate individual RGCs of the major types with single-cell, single-spike resolution (Sekirnjak et al., 2008; Jepson et al., 2013, 2014b), and that the distinct cell types can be distinguished by their recorded electrical signatures (Richard et al., 2016; Zaidi et al., 2022; Madugula et al., 2022a), raising the possibility of reproducing the neural code using epiretinal stimulation. More recently, a stimulation algorithm was developed to optimize the quality of vision restoration in conditions when stimulation is focal and precisely calibrated but imperfect (Shah et al., 2019b, 2022). However, it remains unclear whether these approaches can be applied effectively to the central retina, the principal target for electronic implants, because the properties and functional organization of the diverse RGC types and the achievable specificity of electrical stimulation in areas of high RGC density are not well understood.

Here, we test how effectively electrical stimulation can reproduce the neural code of two major RGC types in the central retina and perform a direct comparison to the peripheral retina. First, using large-scale multielectrode recordings and visual stimulation, we probe the functional organization, light responses, spiking, and electrical properties of four numerically dominant RGC types—ON parasol, OFF parasol, ON midget, and OFF midget (Dacey, 2004)—in the raphe region of the central macaque monkey retina (eccentricity, 4.5–20°). Next, we record and stimulate ON parasol and OFF parasol cells in the raphe and demonstrate that these two cell types can be identified and distinguished from midget cells based solely on their recorded electrical signatures, and can be activated with high spatial and temporal precision. Third, we use responses to electrical stimulation in parasol cells to estimate the visual signal reproduction that is possible with a central-targeting implant that algorithmically optimizes electrical stimulation (Shah et al., 2019b, 2022). Although the selectivity of stimulation was lower in the central compared with the peripheral retina, the unwanted activation of axons was reduced, and the overall expected image quality from parasol cells was substantially higher. These results support the possibility of high-fidelity vision restoration in the central retina with an epiretinal implant.

Materials and Methods

Experimental procedures. Eyes were obtained from terminally anesthetized macaque monkeys (*Macaca mulatta, Macaca fascicularis*) of either sex (32 males, 6 females) used by other researchers, in accordance with Institutional Animal Care and Use Committee guidelines. Immediately after enucleation, the eye was hemisected in room light and the anterior portion of the eye and the vitreous humor was removed. The posterior portion of the eye was stored in oxygenated, bicarbonate-buffered Ames' solution (Sigma-Aldrich) at 31–33°C.

In infrared or dim lighting, small ($\sim 2 \times 2$ mm) segments of retina, along with the attached retinal pigment epithelium (RPE) and choroid, were separated from the sclera. In most preparations, the retina was then separated from the RPE; in one preparation (Fig. 1B), the RPE was left attached. The retina was placed RGC side down on a custom high-density multielectrode array, and a transparent dialysis membrane was used to press the retina against the array from the photoreceptor side. A total of 52 retinal preparations was used: 15 from the raphe region and 37 from the periphery. For raphe preparations, regions 1–4.5 mm (4.5–20°) eccentricity along the temporal horizontal meridian were obtained. For peripheral preparations, segments in both temporal and nasal regions of the retina were obtained, with eccentricities ranging from 5 to 12 mm in eccentricity (22–56° temporal equivalent). Once the retina was mounted on the array, it was superfused with oxygenated, bicarbonate-buffered Ames' solution at 32–35°C.

Visual stimulation and recording. The retina was typically stimulated with a white noise visual stimulus from a gamma-corrected cathode ray tube monitor refreshing at 120 Hz. The three monitor primaries were modulated independently for spectral variation, or in a coordinated manner for a black-and-white stimulus. The stimulus refresh interval was either 8.37, 16.74, or 33.47 ms and the size of each stimulus pixel at the photoreceptor layer ranged from ~ 22–$176\,\mu m$. For a single preparation (Fig. 1B), the retina was stimulated with a gamma-corrected organic light-emitting diode monitor refreshing at 60 Hz. In this case, the stimulus refresh interval was 16.57 ms and the size of each stimulus pixel at the photoreceptor layer was $\sim 36\,\mu m$. The recordings were obtained using a custom multielectrode stimulation and recording system with 512 electrodes (diameter, 5–15 μm) with either 30 μm pitch, covering an area of 0.43 mm², or 60 μm pitch, covering an area of 1.7 mm² (Litke et al., 2004; Hottowy et al., 2008, 2012). Raw signals from the channels were amplified, filtered (43–5000 Hz), multiplexed, digitized at 20,000 Hz, and stored for off-line analysis, as described previously (Litke et al., 2004). KiloSort (Pachitariu et al., 2016) was then applied to the raw recordings to separate and identify unique cells and their spike times.

Cell type classification. To classify distinct cell types based on their light response properties, the spike-triggered average (STA) was computed for each cell (Chichilnisky, 2001). The receptive field (RF) of each cell was estimated by determining the pixels within the STA with a signal significantly above the noise level (Gauthier et al., 2009a). The time course of the STA was computed by summing the primaries of pixels within the RF. The spatial component of the STA was computed for each cell by taking the inner product between the time course and the full STA, and the output was fitted with a 2D Gaussian. Clusters of light response properties (RF diameter, first principal component of time course; Fig. 1) and spiking properties (first principal component of the spike train autocorrelation function; see below) were used to identify distinct cell types (Field et al., 2007). Recordings in most peripheral and some central retina preparations typically revealed the five numerically dominant RGC types: ON parasol, OFF parasol, ON midget, OFF midget, and small bistratified. In most preparations, recordings from ON and OFF parasol cells were nearly complete, whereas recordings from ON and OFF midget and small bistratified cells were less complete (Fig. 1).

Linear–nonlinear Poisson cascade model. To summarize the light response properties of the major RGC types, the linear–nonlinear Poisson (LNP) cascade model was fitted to responses to white noise (Chichilnisky, 2001; Chichilnisky and Kalmar, 2002). At the retinal eccentricities recorded, the RF diameters of raphe RGCs are approximately half the diameter of those in the periphery (Figs. 1, 2). Therefore, to compare model parameters in the raphe and periphery, stimuli with a 22 μm pixel width were used in the raphe and stimuli with a 44 or 55 μm pixel width were used in the periphery. Both stimuli had a 16.74 ms refresh interval. Preparations recorded at different
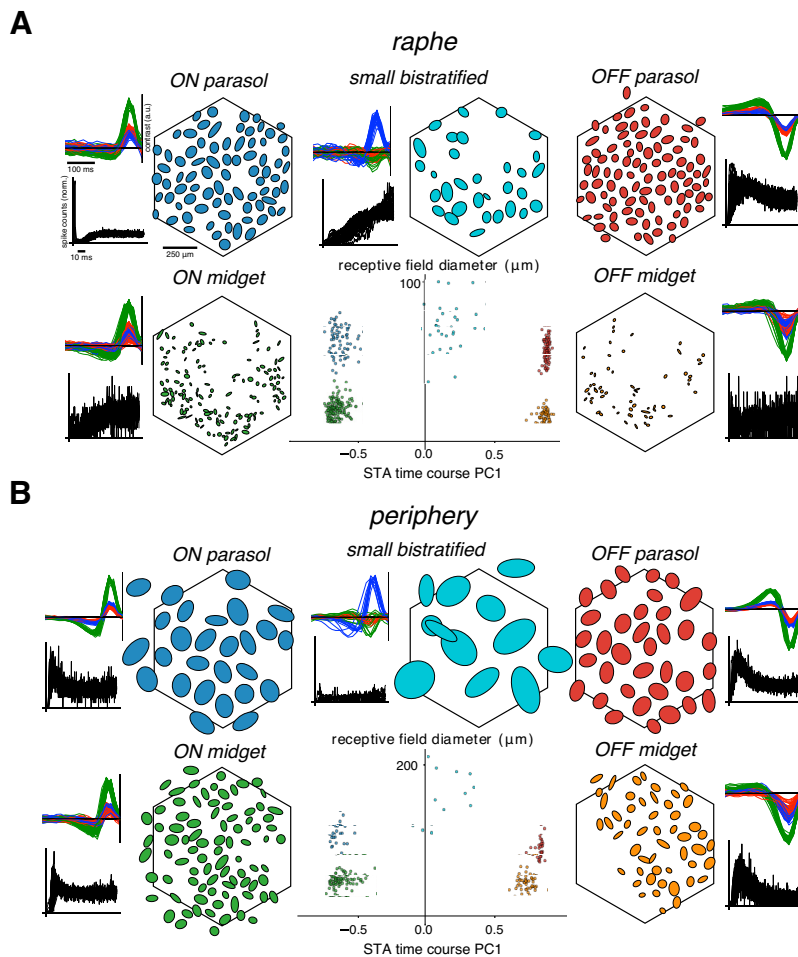
Figure 1. Identification of major RGC types using light response and spiking properties in the raphe and peripheral retina. ***A***, Example recording from the raphe (eccentricity, 3.5 mm). Clusters of RF diameter and the first principal component (PC1) of the STA time course (and occasionally the PC1 of the spike train autocorrelation function; data not shown) were used to separate and identify known functionally distinct cell types. The RF mosaics, STA time courses, and spike train autocorrelation functions are shown for each cell type. The ellipses denote the 2σ boundary of a 2D Gaussian fit to the spatial component of the STA. Note: other cell types were also observed, forming different clusters, but for clarity, data only for the five numerically dominant RGC types—ON parasol, OFF parasol, ON midget, OFF midget, and small bistratified—are shown. Black hexagonal outline denotes the approximate location of the electrode array. ***B***, Same as ***A***, but for an example recording in the peripheral retina (8.5 mm temporal equivalent eccentricity).

logarithm of the ratio of $f'(x_{+\sigma})$ and $f'(x_{-\sigma})$, where $f'(x)$ is the first derivative of the contrast–response relation at x (computed numerically using the central difference method) and x_σ is the 1 SD generator signal value estimated from the distribution of all generator signal values for that cell during the recording.

Analysis of spike train autocorrelation functions. The autocorrelation function of the spike trains from white noise visual stimulation were computed for each parasol and midget cell. Briefly, spike times were binned with 1 ms precision and a histogram of pairwise spike time differences (range, 1–500 ms) was calculated and then the spike counts within each bin were then converted to a spike rate. To determine differences in firing between raphe and peripheral parasol cells, the autocorrelation was normalized to unit sum and the sum of the first 25 elements (1–25 ms) for ON parasol cells and the first 100 elements (1–100 ms) for OFF parasol cells was calculated. These quantities provide estimates of the probability that, after the occurrence of a spike, a second spike occurs within 25 and 100 ms, respectively.

Analysis of spike train cross-correlation functions. The cross-correlation functions of spike trains obtained during white noise visual stimulation were computed between all homotypic pairs of ON parasol and OFF parasol cells. Briefly, spike times were binned with 1 ms precision and a histogram of pairwise spike time differences ranging from −1000 to 1000 ms (0 ms inclusive) was calculated, and then the spike counts within each bin were converted to a spike rate. To determine differences in correlated firing kinetics, nearest-neighbor homotypic pairs of ON parasol and OFF parasol cells were identified and an estimate of the baseline spike rate was determined by calculating the median value of the spike rate from −1000 to −995 ms time offset and from 995 to 1000 ms time offset. Next, the cross-correlation was smoothed with a Gaussian kernel ($\sigma = 5$ ms), the noise estimate was subtracted, and the resulting signal was upsampled 10×. To determine the width of the cross-correlation, the full-width at half-maximum (FWHM) was computed.

Analysis of receptive field overlap. To determine the RF overlap between nearest-neighbor homotypic pairs of ON and OFF parasol cells, an estimate of the RF of each RGC was generated from its 2D Gaussian fit and the correlation coefficient between the RF of each cell and the RF of its nearest homotypic neighbor.

Analysis of electrical images. Electrical images (EIs) were computed for each cell by averaging the voltage signal on the array during the time of each spike (Litke et al., 2004; Petrusca et al., 2007). Features of spike waveforms obtained from the EI were then used to classify them into distinct cellular compartments (Litke et al., 2004; Müller et al., 2015). In general, somatic and dendritic waveforms exhibit biphasic structure, whereas axonal waveforms exhibit triphasic structure, reflecting biophysical differences between compartments. Based on these known differences, a heuristic-based automated method (Madugula et al., 2022b) was applied to label each electrode as either "dendritic," "somatic," "axonal," or "mixed" (a superposition of either somatic and dendritic or somatic and axonal waveforms; Madugula et al., 2022b). First, waveforms with a larger positive than negative phase were labeled as dendritic. Second, the waveforms at remaining electrodes were identified as somatic, mixed, or axonal, based on the ratio of the first positive peak to the second positive peak. Thresholds for each respective compartment were determined by two empirically observed inflection points (0.05 and 1.6, respectively) in the pooled distribution of ratios obtained from many cells and electrodes in peripheral recordings.

temperatures (32, 33, and 35°C) were all used, and there was a modest effect of temperature (i.e., lower temperatures resulted in slightly slower response time courses). However, the effects reported here were present at all temperatures (albeit with different magnitudes), and thus are not attributable to temperature differences.

First, the RF diameter of each cell was determined by fitting a 2D Gaussian to the spatial component of the STA (see above) and calculating the geometric mean of each SD parameter multiplied by 2. To summarize the response time course of each cell, the STA time course of each cell was normalized (L2) and fitted with a difference of cascades of low-pass filters of the form $f(t) = p_1(t/\tau_1)^n e^{-n(t/\tau_1-1)} - p_2(t/\tau_2)^n e^{-n(t/\tau_2-1)}$, where $f(t)$ is the time course, t is the time index, and n, p_1, τ_1, p_2, and τ_2 are free parameters (Chichilnisky and Kalmar, 2002). Then, the time of zero crossing of the time course was estimated by numerically solving for the root of the fitted function using the bisection method. Last, the contrast–response relationship for each cell was estimated from the STA, stimulus, and spike train (Chichilnisky, 2001; Chichilnisky and Kalmar, 2002) and fitted with a smooth function of the form $f(x) = \alpha L(\beta x + \gamma)$, where x is the generator signal, L is the logistic cumulative distribution function, and α, β, and γ are free parameters. The nonlinearity index for each cell was defined as the

To determine spike amplitudes within each compartment, for each cell, electrodes recording somatic and axonal signals were determined and the maximum absolute value of the peak negative voltage on each electrode was calculated. Then, the maximum voltage over somatic and axonal electrodes was computed. Each preparation in this analysis was acquired using the electrode array with 30 μm interelectrode spacing to ensure consistent estimates of spike amplitudes (see Fig. 4B).

Axon spike conduction velocity was estimated from the electrical images of ON and OFF parasol and midget cells, as described previously (Zaidi et al., 2022; Madugula et al., 2022a). Briefly, axonal electrodes for each cell were identified (see above) and pairwise velocity estimates were computed by dividing the distance between each electrode by the time difference in the negative peak amplitude, for each pair of axonal electrodes. Then, a velocity estimate was computed by averaging the estimate from each pair of electrodes weighted by the product of the peak amplitudes.

Analysis of electrical features for distinguishing cell types. Axon spike conduction velocities and the spike train autocorrelation function were used together to distinguish ON and OFF parasol and ON and OFF midget cells, to demonstrate the effectiveness of cell type classification based on intrinsic electrical features alone (Richard et al., 2016; Zaidi et al., 2022). Each preparation in this analysis (see Fig. 4C–G) was acquired using the electrode array with 30 μm interelectrode spacing to ensure consistent estimates of spike conduction velocities. To quantify the degree of separability between parasol and midget cell spike conduction velocities, a 1D support vector machine was fitted to the spike conduction velocity–cell type label pairs (L2-penalty with a linear kernel). The learned optimally separating hyperplane (a point in the 1D space) was used to quantify the classification accuracy on the training data. The goal of this analysis was merely to determine the degree of separability in the data, so cross-validation with held-out data was not performed.

Parasol and midget cells were highly distinguishable using spike conduction velocity (see Fig. 4D,F). To determine whether ON and OFF types within the parasol and midget cell classes could be separated by features of the autocorrelation function, the autocorrelation function was calculated (see above), and the resulting spike count vector was normalized by its L2 norm. Then, principal components analysis (PCA) was performed on a data matrix composed of either ON and OFF parasol or ON and OFF midget cell autocorrelation functions, and projections onto the first two principal components were analyzed (see Fig. 4E,G, insets). To quantify the degree of separability between ON and OFF (parasol or midget) spike train autocorrelation functions, a 2D support vector machine was fitted to the projections onto the first two principal components along with the corresponding cell type labels (L2 penalty with a linear kernel). The learned optimally separating hyperplane (a 1D
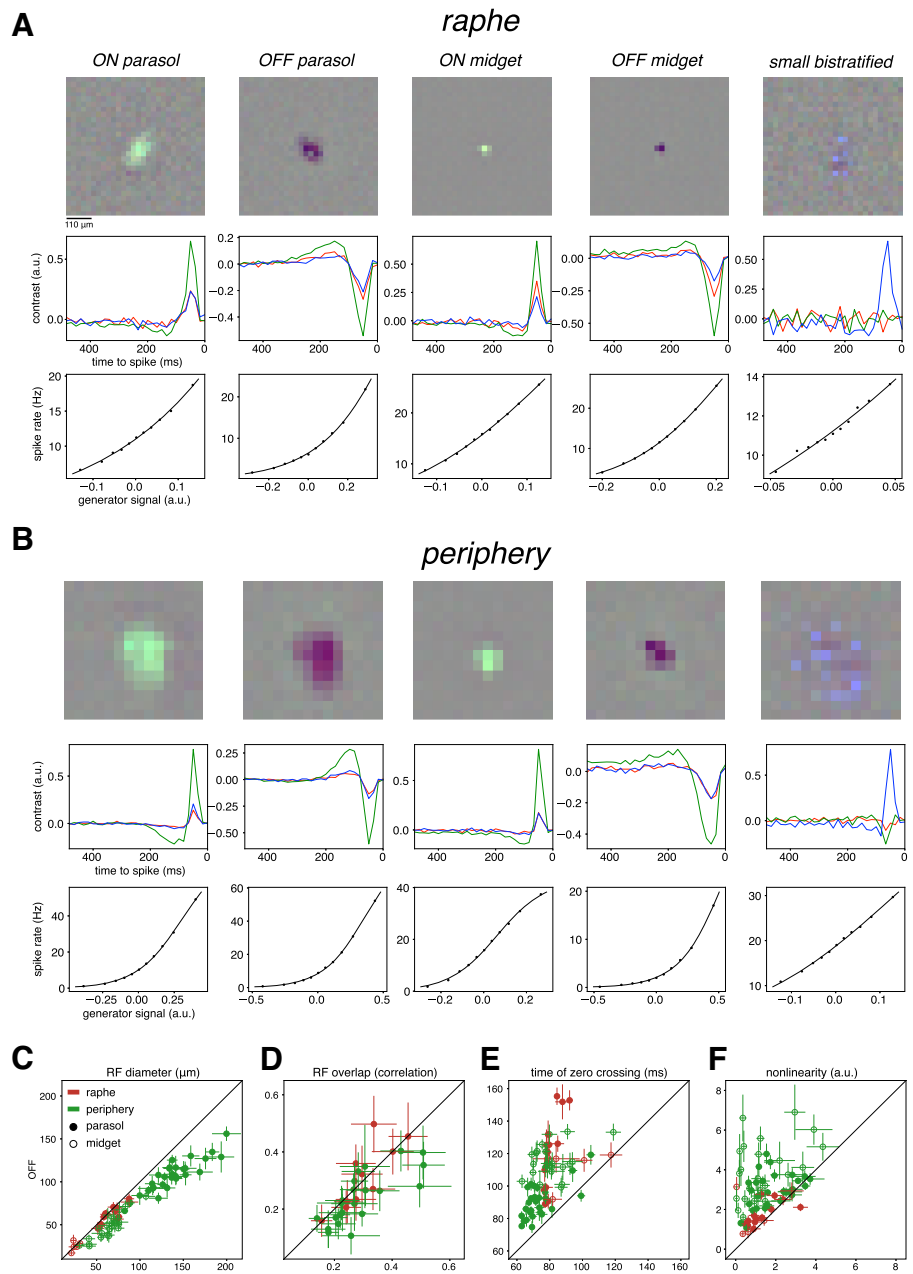
Figure 2. LNP model comparison between raphe and peripheral RGCs. **A**, Example spatial component of the STA (top), STA time course (middle), and contrast–response relationship (bottom) for each of the five numerically dominant cell types in a single raphe preparation. **B**, Same as **A** but for a peripheral preparation. **C–F**, Comparisons of RF diameter (**C**), RF overlap (**D**; see Materials and Methods), time of zero crossing of STA time course (**E**), and nonlinearity index extracted from the contrast–response relation (**F**; see Materials and Methods) between raphe and peripheral ON and OFF parasol and midget cells. Each data point represents the median value ($\pm$1 median absolute deviation) from a single preparation.

line in the 2D space) was used to quantify the classification accuracy on the training data. As above, cross-validation with held-out data was not tested.

Responses to electrical stimulation. To identify the responses to electrical stimulation of each recorded RGC, a current pulse was delivered to each electrode on the array, in a random sequence across electrodes, while recording RGC responses on all electrodes simultaneously (Jepson et al., 2013; Grosberg et al., 2017). The pulse was triphasic, positive first, and charge balanced (50 μs/phase; relative ratios, 2:–3:1). The current amplitude range tested (second phase) was 0.1–4.1 μA ($\sim$40 amplitudes, logarithmic scale), with each amplitude repeated 25 times. In all electrical stimulation experiments, the electrode array with 30 μm interelectrode spacing was used.

An automated spike-sorting method was used to identify RGC responses to electrical stimulation. First, for each stimulating electrode, RGCs were identified as candidates for electrically evoked activity if their EIs (obtained during visual stimulation) exhibited peak amplitudes >0.5 times the SD of the recorded electrical noise on that electrode. Each RGC was then assigned a set of significant electrodes from its EI recording signals with power greater than two times the power of electrode noise on each electrode to be used to determine responses. Cells that did not have at least one electrode with signal power greater than two times the power of the electrical noise threshold were excluded from analysis because their signals could not be distinguished from noise. Then, for each current amplitude, across all RGCs and their respective significant electrodes, voltage traces recorded in the 3 ms period following stimulus application were grouped using unsupervised clustering. For each pair of clusters, signals were subtracted, aligned, and averaged to obtain differences; typically, these difference signals reflect the firing of one or more cells in one cluster but not the other. These residuals were iteratively compared with each of the recorded spike waveforms obtained from the EIs of all RGCs and their respective significant electrodes to identify the set of RGCs contributing to the responses in each trial for each amplitude.

This algorithm produces response probabilities as a function of current level, for each RGC and stimulating electrode, which is in general monotonically increasing (Hottowy et al., 2012; Jepson et al., 2013). The relationship between current amplitude and response probability for each RGC and stimulating electrode was then fitted by a sigmoidal curve of the form $p(a) = \dfrac{1}{e^{-k(a-b)}}$, where $p(a)$ is the probability of activation, a is the current amplitude, and k and b are free parameters, using maximum likelihood estimation. The stimulation threshold (i.e., the current amplitude required to elicit a response probability of 0.5) was extracted from the fit (Jepson et al., 2013).

Analysis of activation thresholds. To determine activation the threshold within each compartment, for each cell, electrodes recording somatic and axonal signals were determined (see above) and the activation threshold for each electrode was extracted from the sigmoidal fit. Then, the minimum activation threshold was computed over somatic and axonal electrodes, for each cell.

Identification of axon bundle activation thresholds. Axon bundle activation thresholds on each electrode were determined by an automated method based on a previously described algorithm (Tandon et al., 2021). The algorithm was modified to avoid bias resulting from differences in array geometries (the present work used a smaller, hexagonal array, whereas the algorithm described in the study by Tandon et al., 2021, was developed using a larger, rectangular array) and axon spike amplitude differences between central and peripheral RGCs (see Fig. 4B). For each preparation, a threshold voltage was first determined to identify electrodes that recorded significant axonal signals in response to electrical stimulation, as follows. For each RGC recorded during white noise visual stimulation, the electrodes recording axonal signals were identified as described above, and the average axonal spike amplitude was determined. The median axonal spike amplitude across all recorded RGCs was computed and was taken to be the threshold voltage. Next, to determine the axon bundle activation threshold, for each stimulus current applied, electrodes were first identified as either recording a signal or not, depending on whether the recorded signal was above the threshold voltage. Activity on the array was identified as an axon bundle activation event when the collection of electrodes recording signals formed a contiguous path reaching at least two nonadjacent edges of the electrode array. The bundle activation threshold was then defined as the minimum current level at which an axon bundle activation event was evoked. Electrodes near the border of the array (outermost two rings of electrodes) were excluded from analysis because their proximity to the edge precludes the ability to unambiguously distinguish RGC activity from axon bundle activity.

Analysis of selectivity. To summarize the selectivity of electrical stimulation, a selectivity metric was computed for each ON and OFF parasol cell. First, at each stimulating electrode, the response probability at each current level below axon bundle activation threshold was determined for the target cell (p_{target}) and every other nontarget parasol cell ($p_{nontarget}$). Then, the maximum value over current amplitudes of the quantity (p_{target}) (1 − $p_{nontarget}$) was determined. This was repeated for each nontarget cell, and the minimum value of (p_{target}) (1 − $p_{nontarget}$) over nontarget cells was determined at this stimulating electrode, to provide a worst case estimate of stimulation selectivity for this cell, at this stimulating electrode. This was repeated for each stimulating electrode, and the maximum value of (p_{target}) (1 − $p_{nontarget}$) over stimulating electrodes was defined as the selectivity index for the cell.

Inference of visual perception. To estimate the quality of restored vision that could be achieved with the measured responses to electrical stimulation, a recently developed stimulation algorithm (Shah et al., 2019b, 2022) was applied in a data-driven simulation. This method assumes that the brain reconstructs visual stimuli from RGC spike trains linearly and optimally, and that responses from individual RGCs that occur within a single "integration time window" of downstream visual processing (e.g., tens of milliseconds) are summed linearly to produce perception.

In this framework, an optimal linear reconstruction filter is associated with each RGC that quantifies its contribution to the image reconstruction each time it fires a spike. To compute the optimal reconstruction filter for each cell, parameters from the LNP model were used to generate responses to white noise images displayed for 100 ms. Specifically, the spike rate was simulated by taking an inner product between the STA and the stimulus and rectifying the result. The STAs were scaled such that the average parasol cell spike rate matched that observed experimentally (approximately three spikes on average per 100 ms flash in the peripheral retina). The stimuli are denoted by the matrix $S \in \mathbb{R}^{images \times pixels}$, and the responses in a matrix $R \in \mathbb{R}^{images \times cells}$. A reconstruction matrix, $W \in \mathbb{R}^{cells \times pixels}$, was computed using linear least-squares regression, via the normal equations: $W = (R^T R)^{-1} R^T S$. In this framework, the brain reconstructs an estimate of the true stimulus S from the RGC responses R by the linear operation $\hat{S} = RW$ (Warland et al., 1997). A single set of reconstruction filters was learned for a set of white noise images with varying pixel sizes (352, 220, 176, 110, 88, and 55 μm), using 10,000 training images each (60,000 images total) to test performance at a range of spatial frequencies. To produce linear reconstruction filters for naturalistic stimuli (Brackbill et al., 2020), this procedure was repeated with 60,000 grayscaled naturalistic images from the ImageNet database (Fei-Fei et al., 2009).

To determine the reconstruction that could be achieved with the responses to electrical stimulation, RGC response probabilities for each cell–electrode pair, at current levels below the threshold for axon bundle activation, were assembled in a matrix, $D \in \mathbb{R}^{cells \times (electrodes \times amplitudes)}$, where the columns are distinct electrical stimuli and the rows are the responses of each recorded cell. The electrical stimulus delivered at each time step was chosen such that the change in the image reconstruction due to the evoked responses of RGCs would maximally reduce the expected mean-squared error (MSE) between the reconstructed image and the target image (Shah et al., 2019b, 2022). The algorithm sequentially chooses stimuli greedily at each time step to minimize the expected MSE until no further reduction in error occurs. No two stimuli resulting in a cellular response probability of >0.04 were delivered within 5 ms of each other to avoid the refractory period, and each stimulation pulse was assumed to be 150 μs in duration, to be consistent with the experimental data and hardware configuration. This method was applied to a total of 90 white noise images (15 for each pixel size) and 100 naturalistic stimuli from the ImageNet database (Fei-Fei et al., 2009), all separate from the images used for training the linear reconstruction filters.

To approximate the optimal reconstruction, or the reconstruction that could be achieved with perfect control over the activity of each RGC, a convex solver was used to solve for the optimal non-negative responses under squared loss between the reconstruction and the true stimulus. This response vector was then discretized by rounding each floating point response to the nearest integer value. Then, for each stimulus, the resulting response vector was applied to the reconstruction matrix to produce the approximate optimal reconstruction.

Convolutional autoencoder. To enhance reconstructions of naturalistic images, a previously described convolutional autoencoder (CAE; Parthasarathy et al., 2017) was applied to linear reconstructions. The CAE was developed as follows. First, linear reconstruction filters were learned for each cell using least-squares regression (see above) on a set of 60,000 training images from ImageNet (Fei-Fei et al., 2009). Then, linearly reconstructed images were generated for each image in the training set using the LNP model generated responses and reconstruction filters. This linear reconstruction was then passed through an eight-layer convolutional neural network with four downsampling layers and four upsampling layers. The Adam optimizer (Kingma and Ba, 2014) with MSE loss and a learning rate of 0.0004 was used for model training. A validation set of 1000 images from ImageNet unseen by both the linear model and the CAE was used to evaluate model accuracy. Twenty training epochs with a batch size of 32 were used, after which validation error did not substantially decrease further.

Analysis of image reconstructions. To quantify the quality of the white noise image reconstructions, two quantities were calculated. First, the set of all relevant pixels was determined for each preparation, indicating the regions covered by the RFs of all ON and OFF parasol cells. Then, the normalized MSE (NMSE) was determined by calculating the squared error between the reconstructed and original images over this set of relevant pixels and normalizing by the squared L2-norm of the original image within this set of pixels.

Next, the fraction of reconstructed pixels with polarities opposite that of the original stimulus was calculated. A subset of the aforementioned set of relevant pixels was determined, indicating regions covered by the RFs of ON and OFF parasol cells chosen to be stimulated by the algorithm. Then, in each reconstructed image, the polarity of each pixel in the reconstruction was compared with that in the original stimulus and the fraction of pixels with opposing polarities was calculated. For the naturalistic image reconstructions, in addition to NMSE, SSIM, a perceptual similarity metric (Wang et al., 2004; Wu et al., 2022), was used to quantify image quality in a way that takes image structure into account. Note that in some of the peripheral preparations (see Fig. 7B), SSIM was slightly larger for empirical naturalistic image reconstructions compared with optimal reconstructions after (but not before) applying the CAE. This is possible because the objective function for optimization in training the CAE was MSE, rather than SSIM. Separately, unlike in the raphe, the CAE had little effect on image reconstructions in some peripheral preparations because their respective linear reconstructions were coarse, because of the relative low density of RGCs.

Simulated midget cell receptive fields and reconstruction filters. To determine the extent of midget cell activation and the noise corruption of reconstructions that would occur when targeting only parasol cells, a raphe preparation with partial recordings of midget cells was used to simulate the electrical stimulation and visual responses of complete populations of ON and OFF midget cells (see Fig. 8A–C). First, RF centers were generated from a hexagonal lattice. Ideally, the spacing of the lattice would be informed by the typical neighbor distance distribution of the midget cells. However, the midget cell populations from each raphe preparation were too sparse to reliably estimate the typical neighbor distance (Fig. 1A; see also Fig. 7A). Since the typical neighbor distance is proportional to the typical RF diameter (Gauthier et al., 2009b), the ON (or OFF) midget cell typical neighbor distance was therefore estimated by computing the median ON (or OFF) parasol typical neighbor distance and scaling this quantity by the ratio of median ON (or OFF) midget cell receptive field diameter to the median ON (or OFF) parasol cell receptive field diameter. This value was used to set the spacing of the lattice. The lattice locations were then jittered by adding Gaussian noise to each x and y coordinate independently, with mean 0 and SD equal to 10% of the original lattice spacing. Next, using the partial populations of ON or OFF midget cells, kernel density estimates were fitted to distributions of the larger of the two (major) SD parameters from the Gaussian fit to the RFs, the ratio of the major SD to minor SD parameters, and the tilt of the receptive fields, across all ON or OFF midget cells. To avoid extreme values, the kernel density estimate was fitted to the subset of the data within the 30th and 70th percentile of each distribution. Receptive fields were then generated by randomly sampling SD parameters and

tilts from the fitted kernel density estimates, resulting in simulated receptive field mosaics (see Fig. 8B).

Next, STAs were generated using the Gaussian parameters from the simulated receptive fields. As with the parasol cells above, the STAs were scaled such that simulated responses to white noise resulted in, on average, three spikes within the simulated ON and OFF midget cell population, consistent with empirical results from parasol and midget cells in the periphery during flashed white noise visual stimulation (data not shown). Using least squares, a set of white noise linear reconstruction filters was learned using 60,000 training images (10,000 from each pixel size), and a set of naturalistic image reconstruction filters was learned using 60,000 training images from the ImageNet database (Fei-Fei et al., 2009).

Simulated midget cell responses to electrical stimulation. To estimate responses to electrical stimulation, recordings during single-electrode stimulation of the partial raphe midget cell populations were analyzed similarly to the parasol cells (see above) by determining response probability as a function of current amplitude and fitting a sigmoid to the resulting relationship, for each cell-electrode pair. For each cell–electrode pair, the bivariate relationship between response probability and soma distance from electrode and current amplitude was determined. This was repeated for each cell–electrode pair, and the data were pooled over all cell–electrode pairs. From the pooled data, the cell–electrode distances and current amplitudes were binned and the average response probability within each bin was calculated, providing a lookup table for a response probability, given a distance from the stimulating electrode and current amplitude (see Fig. 8C).

Estimation of midget cell noise. The electrical stimuli provided to the parasol cells for the white noise reconstruction simulation (see Fig. 6A, B) were then used to generate expected responses for each simulated midget cell. Specifically, for each electrical stimulus and cell, the distance from the electrode and the current amplitude were used to determine the response probability (see Fig. 8C). Over the entire stimulation sequence, the expected response for each midget cell would therefore be the sum of the probabilities from each stimulus. The resulting expected response vector was then passed as input to the linear decoder, yielding the midget cell reconstruction. Finally, this resulting reconstruction was summed with the parasol reconstruction to obtain an estimate of the expected perception when midget cells are ignored during parasol cell stimulation (see Fig. 8D).

Early stopping criterion. To reduce the magnitude of midget cell activation and consequent noise added to white noise reconstructions, an early stopping procedure was developed based on an estimate of the midget cell noise. In its original form, the stimulation algorithm used here (Shah et al., 2019b, 2022) continues to provide electrical stimuli greedily until no further reduction in expected MSE between the target stimulus and the expected parasol cell reconstruction can be achieved. In the modified procedure, the MSE between the target image and the reconstruction with the midget noise added is calculated at each electrical stimulus, and the "early stopping point" is defined as the stimulation number at which the global minimum in MSE is achieved. The exact optimal early stopping point is unknown, and its estimation is directly affected by the estimate of the midget cell population, which is based on the true population, but is simulated and stochastic. To minimize potential bias in the early stopping point, 10 distinct midget cell populations were generated as above using 10 different seeds for the receptive field and electrical stimulation response generation. Then, the early stopping point for each midget cell population was determined for each of the 90 white noise stimuli, and the median stopping point across the midget cell populations was calculated for each stimulus. Then, a distinct midget cell population was used for evaluation (see Fig. 8B–D,F) using the early stopping points determined from the separate "training" midget cell populations.

Analysis of noise contributed by midget cells. To quantify the extent of image corruption by the activation of midget cells, fractional error was calculated as error$_{parasol+midget}$/error$_{parasol}$, where error$_{parasol+midget}$ is the error of the reconstruction with midget cell noise added to the parasol cell signals and error$_{parasol}$ is the error of the reconstruction from parasol cells only. For white noise images, error was either the root MSE

(RMSE) or the fraction of incorrect pixels. For naturalistic images, error was either RMSE or 1 - SSIM.

Experimental design and statistical analyses. In nearly all statistical tests, a two-tailed Mann–Whitney U test was performed using the statistics package in SciPy (Virtanen et al., 2020). In the statistical test comparing the fraction of RGCs that could be activated with a probability of 0.5 without activating axon bundles (see Fig. 5B), a custom resampling procedure was implemented. All p values $\geq 1 \times 10^{-10}$ are reported as exact values; all others are reported as $p < 1 \times 10^{-10}$.

Results

To understand the quality of vision restoration that could be achieved with an electrical implant in the central retina, we performed recording and stimulation *ex vivo* in the macaque monkey retina with large-scale multielectrode arrays and determined how accurately visual stimuli can be represented in electrically evoked RGC activity.

Identification of the major RGC types in the central retina
To determine the functional organization of major RGC types in the central retina, light responses were obtained from regions of macaque retina 1–4.5 mm from the fovea along the temporal horizontal meridian, in the raphe region (Vrabec, 1966), where few multielectrode recordings have been performed (Grosberg et al., 2017). Recordings from the more commonly studied peripheral retina (temporal equivalent eccentricity, 5–12 mm) were also obtained for comparison. The preparation was visually stimulated with white noise while recording spikes from hundreds of RGCs simultaneously, using an electrode array with 512 electrodes and 30 or 60 μm pitch (Litke et al., 2004). The spike-triggered average (STA) stimulus was computed for each cell, summarizing the spatial, temporal, and chromatic properties of the light response (Chichilnisky, 2001; Chichilnisky and Kalmar, 2002). Cell types were then classified by clustering based on the spatial RF obtained from the STA, the time course of the STA (Fig. 1), and the spike train autocorrelation function (Field et al., 2007; Rhoades et al., 2019).

This approach revealed the five numerically dominant primate RGC types: ON parasol, OFF parasol, ON midget, OFF midget, and small bistratified (Fig. 1), which are readily identified by their light response characteristics and densities relative to other types (Dacey, 2004; Rhoades et al., 2019). Recordings from ON and OFF parasol cells were consistently nearly complete, as evidenced by the mosaic organization of their RFs (Fig. 1). Recordings of ON and OFF midget cells and small bistratified cells were less complete (Fig. 1), particularly in the raphe region (Fig. 1A). As expected, the spatial densities of these five cell types in the raphe (Fig. 1A) were higher than those of the corresponding cell types in the peripheral retina (Fig. 1B).

Neural code of the major RGC types in the central retina
Visual signals in RGCs are often modeled using a simple cascade model, consisting of a spatiotemporal linear filter, a nonlinearity, and Poisson spiking statistics (Rodieck, 1965; Meister and Berry, 1999; Chichilnisky, 2001; Pillow et al., 2008). To compare visual processing in the raphe and periphery, this LNP model was fitted to RGC responses to white noise (Chichilnisky, 2001; Chichilnisky and Kalmar, 2002), and the spatial RF, response time course, and contrast–response relationship from the fitted models were examined (Fig. 2). The spatial RFs of RGCs in the raphe were on average smaller than those of their peripheral counterparts for both

parasol (Fig. 2C, Mann–Whitney U test: ON and OFF, $p < 1 - \times 10^{-10}$) and midget cells (Fig. 2C; Mann–Whitney U test: ON and OFF, $p < 1 \times 10^{-10}$), as expected from the smaller dendritic fields and higher density in the central retina (Watanabe and Rodieck, 1989; Dacey and Petersen, 1992). In addition, the RF overlap (see Materials and Methods) of nearest-neighbor ON and OFF parasol cells was significantly higher in the raphe (Fig. 2D; Mann–Whitney U test: ON, $p = 0.002$; OFF, $p < 1 \times 10^{-10}$). The response time course was slower in central than peripheral parasol cells (Fig. 2E; Sinha et al., 2017), Mann–Whitney U test: ON and OFF, $p < 1 \times 10^{-10}$) with a more pronounced ON–OFF asymmetry (Chichilnisky and Kalmar, 2002). The time courses of central ON midget cells were significantly slower than those of peripheral ON midget cells (Fig. 2E; Mann–Whitney U test, $p < 1 \times 10^{-10}$). However, no significant difference between central and peripheral OFF midget cell time courses was observed (Mann–Whitney U test, $p = 0.35$), perhaps because of the small number of recorded OFF midget cells in the raphe. The contrast–response relationship was more linear (see Materials and Methods) in raphe parasol cells (Fig. 2F; Mann–Whitney U test: ON and OFF, $p = < 1 \times 10^{-10}$) and midget cells (Mann–Whitney U test: ON, $p = 7.05 \times 10^{-10}$; OFF, $p < 1 \times 10^{-10}$), with a weaker ON–OFF asymmetry (Chichilnisky and Kalmar, 2002).

To test whether the spike timing structure of central versus peripheral RGCs differs, the autocorrelation function of the spike train obtained during white noise stimulation was examined. Peripheral ON parasol cells tended to have an early peak in the autocorrelation at ~2–5 ms, indicative of frequent doublet firing (Fig. 3A, left), compared with the more gradual increase over tens of milliseconds for raphe ON parasol cells (Fig. 3A, left). Compared with peripheral cells, the normalized early spike count (1–25 ms; see Materials and Methods) was significantly lower in raphe ON parasol cells (Fig. 3B, left; Mann–Whitney U test, $p < 1 \times 10^{-10}$). Raphe and peripheral OFF parasol cell autocorrelations exhibited the same general shape, but in the raphe the autocorrelations had a significantly higher spike rate within the range of 1–100 ms (Fig. 3A, right), which was captured by the higher normalized spike count (Fig. 3B, right; Mann–Whitney U test, $p < 1 \times 10^{-10}$; see Materials and Methods). These findings reveal potential differences in intrinsic excitability between central and peripheral parasol cells or their synaptic inputs (see Discussion).

To test whether concerted firing between neighboring RGCs differs in the central versus peripheral retina, cross-correlation functions of spike trains obtained during white noise stimulation were computed between homotypic pairs of nearest-neighbor ON and OFF parasol cells (Mastronarde, 1983; Shlens et al., 2006, 2009; Pillow et al., 2008; Trong and Rieke, 2008). Similar to the peripheral retina, raphe ON and OFF parasol cell cross-correlations exhibited a symmetric, smoothly decaying form peaked at the origin (Fig. 3C). However, parasol cell cross-correlations in the raphe were significantly wider (see Materials and Methods) than those in the periphery, particularly for OFF parasol cells (Fig. 3D; Mann–Whitney U test: ON and OFF, $p < 1 \times 10^{-10}$), likely reflecting slower response time courses (Fig. 2E; see Discussion).

In summary, the neural code of major RGCs in the raphe, including light response properties (Fig. 2), spiking statistics (Fig. 3A,B), and concerted firing of neighboring RGCs (Fig. 3C, D), was largely similar to that in the peripheral retina, with some systematic differences in RF density, kinetics, nonlinearity, and firing statistics.
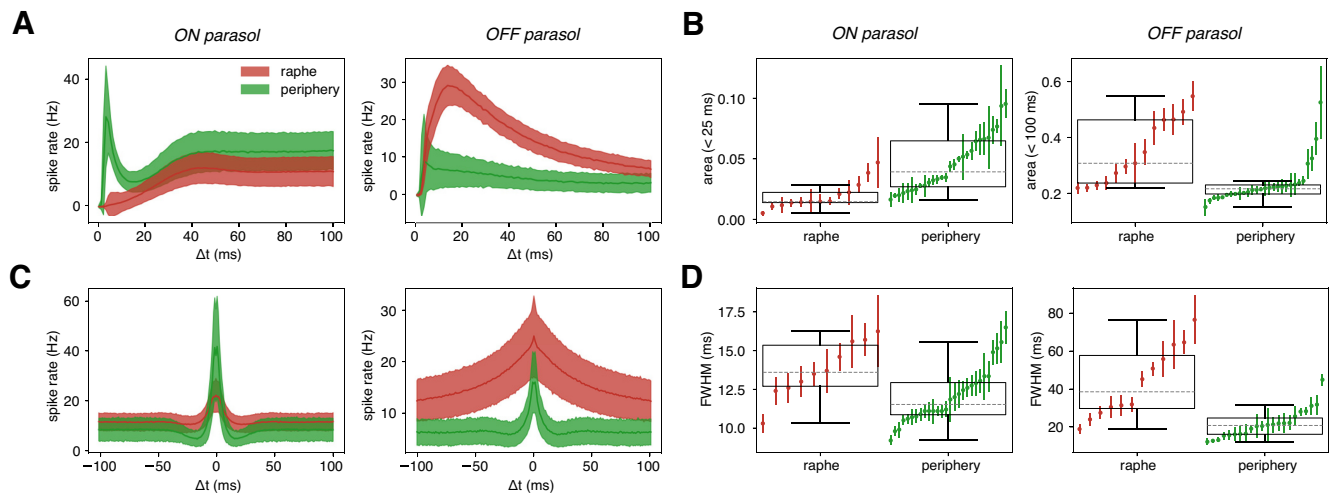
Figure 3. Spiking statistics and correlated firing in ON and OFF parasol cells in the raphe and the periphery. **A**, Mean (±1 SD) spike train autocorrelation functions for ON (left) and OFF (right) parasol cells in one peripheral and one raphe preparation. **B**, Probability of spike within 1–25 ms for ON parasol cell autocorrelations (left) and 1–100 ms for OFF parasol cell autocorrelations (see Materials and Methods). Each data point represents the median (+1 median absolute deviation) value in a single preparation. **C**, Mean (±1 SD) nearest homotypic neighbor spike train cross-correlation functions for ON (left) and OFF (right) parasol cells in one peripheral and one raphe preparation. **D**, FWHM (see Materials and Methods) of nearest homotypic neighbor cross-correlation functions. Each data point represents the median (±1 median absolute deviation) value in a single preparation. In each box plot, the box denotes the interquartile range, the dashed gray line denotes the median value of all points in the plot, and the bottom and top whiskers denote the first quartile minus 1.5 times the interquartile range and the third quartile plus 1.5 times the interquartile range, respectively.

Distinguishing major RGC types using intrinsic electrical features

Reproduction of the neural code with electrical stimulation requires identifying cell types in the absence of light responses (which are degraded or absent during degeneration) as well as measuring the sensitivity of each cell to electrical stimulation (Li et al., 2015; Richard et al., 2016; Shah et al., 2019a; Zaidi et al., 2022; Madugula et al., 2022a, b). To probe these properties, electrical images, or the average spatiotemporal electrical footprint of the spike of a cell (Litke et al., 2004; Petrusca et al., 2007), was examined for the recorded RGCs. Electrical images of simultaneously recorded RGCs in the raphe revealed axons that projected in one of two directions ~90° apart (Fig. 4A, left), consistent with the unique anatomic structure of this region (Vrabec, 1966; Grosberg et al., 2017), whereas in the periphery, the axons of RGCs all projected in the same direction toward the optic disk (Fig. 4A, right). Spike amplitudes were significantly smaller in raphe compared with peripheral parasol cells in both somatic (Mann–Whitney U test, $p < 1 \times 10^{-10}$) and axonal (Mann–Whitney U test, $p < 1 \times 10^{-10}$) cellular compartments (Fig. 4B), likely reflecting the smaller cell bodies and axon diameters in the raphe. Finally, the axon spike conduction velocity (see Materials and Methods) was significantly lower in raphe compared with peripheral parasol cells (Fig. 4C; Mann–Whitney U test, $p < 1 \times 10^{-10}$).

Raphe RGCs exhibited electrical image features and spike train statistics that can support cell type identification. Parasol cells exhibited significantly higher conduction velocities than midget cells (Fig. 4D) and could be distinguished reliably on this basis (94% classification accuracy; see Materials and Methods). Next, within the parasol and midget cell classes, principal components analysis (PCA) on the spike train autocorrelation functions (Fig. 4E) revealed two clearly defined clusters corresponding to the ON and OFF types (Fig. 4E, insets; 100% classification accuracy for ON vs OFF parasol cells; 94% classification accuracy for ON vs OFF midget cells). The degree of cell type separability using these features was comparable to that in the peripheral retina (Fig. 4F,G; 97% classification accuracy for

parasol vs midget cells; 98% classification accuracy for ON vs OFF parasol cells; and 100% classification accuracy for ON vs OFF midget cells).

Selectivity of electrical stimulation of central parasol cells

Because RGCs of different types are intermixed on the retinal surface, accurately reproducing the cell type-specific patterns of activity in the retinal neural code (Roska and Meister, 2013) would typically require stimulation with single-cell resolution. To test whether this is possible in the raphe, spikes were identified in recorded traces immediately after application of a brief current pulse (triphasic, 0.15 ms) at each electrode individually, over a range of current levels (0.1-4.1 µA), repeated 25 times (see Materials and Methods), using the 512-electrode array with 30 µm pitch. These small currents typically directly evoke a single spike in one or more RGCs near the electrode (Sekirnjak et al, 2006, 2008; Jepson et al., 2013). For each recorded cell, the evoked spike probability was calculated at each current level, and a sigmoid fitted to response probability as a function of applied current was used to estimate the activation threshold, i.e., the current that produced a spike with probability 0.5. For each electrode, the axon bundle activation threshold was also examined, using an algorithm that identified bi-directional propagation of electrical activity to the edges of the array, a distinctive signature of axon activation (Grosberg et al., 2017; Tandon et al., 2021; see Materials and Methods). Activation thresholds for individual parasol cells were similar in the raphe and peripheral retina in both their somatic and axonal compartments (Fig. 5A). In addition, a significantly larger fraction of raphe RGCs (78%) could be activated with probability 0.5 without activating axon bundles compared with the peripheral retina (50%, resampled $p < 1 \times 10^{-10}$; Fig. 5B), consistent with a previous finding with more limited data (Grosberg et al., 2017).

To summarize how precisely individual RGCs can be activated, a selectivity index was computed for each parasol cell relative to other parasol cells: $p_{target}(1 - p_{nontarget})$, where p_{target} is the probability of firing of the target parasol cell, and $p_{nontarget}$ is the probability of firing of the most sensitive nontarget parasol cell,

across stimulating electrodes and current levels (see Materials and Methods). An index of 1 indicates perfect selectivity for the target parasol cell over all nontarget parasol cells that could be stimulated by the same electrode used for the target parasol cell. Across eight raphe preparations (Fig. 5C, top two rows), the average selectivity index of all ON and OFF parasol cells within the preparation ranged from 0.59 to 0.79 (Fig. 5D, top two panels). By comparison, the average selectivity in the peripheral retina (Fig. 5D, bottom two rows) was significantly higher (Mann–Whitney U test; ON and OFF parasol cells, $p < 1 \times 10^{-10}$), ranging from 0.84 to 1.0 across preparations (Fig. 5D, bottom two panels). Greater selectivity in the periphery is expected from the lower RGC density, and is consistent with previous findings (Grosberg et al., 2017). In summary, activation of a single parasol cell without activating other recorded parasol cells is often possible in the central retina, but is less frequently achieved than in the peripheral retina.

Inference of high-fidelity visual signal reproduction in the central retina

To determine whether electrical stimulation in the raphe can reproduce high-fidelity visual signals, the ability to reconstruct a visual image from RGC signals was evaluated (Shah et al., 2019b, 2022) in a simulation based on recorded electrically evoked responses. First, to perform efficient image reconstruction, LNP model responses to flashed white noise images were generated, and linear reconstruction filters for each RGC were computed using least-squares regression between the images and model responses (see Materials and Methods; Warland et al., 1997; Brackbill et al., 2020). Then, using the measured electrically evoked responses of each cell at each stimulating electrode and each current amplitude below axon bundle activation threshold (Fig. 5), a spatiotemporal dithering strategy was used to select a pattern of electrical stimulation that would maximally decrease the expected mean-squared error (MSE) between the target image and the image reconstructed from the electrically evoked responses (Shah et al., 2019b, 2022). The simulation produces stochastic RGC responses, and therefore, stochastic reconstructions. In this analysis, the expected reconstruction was examined (see Discussion).

Application of this method revealed substantial differences in reconstruction performance between the raphe and peripheral retina. Compared with the peripheral retina, the optimal reconstructions (i.e., the reconstructions that could in principle be achieved with perfect control over RGC activation) and the empirical reconstructions (i.e., the reconstructions that could be achieved, on average, with measured activation probabilities) in the raphe were both systematically higher quality than those in the peripheral retina, with sharper edges and more distinct regions that more closely matched the structure of the original image (Fig. 6A). This was evident over a range of pixel sizes (Fig. 6B). Although image reconstruction was less faithful at smaller pixel sizes in both the central and peripheral retina (Fig. 6B), image quality in the central retina was still higher at each pixel size examined.

The reconstructed image quality was measured by computing the normalized MSE (NMSE) (see Materials and Methods) between the reconstruction and original image, and the fraction of pixels with incorrect polarities in the reconstruction. In the central retina, both NMSE and the fraction of incorrect pixels were significantly lower compared with the peripheral retina, for each pixel size examined (Fig. 6C; Mann–Whitney U test; NMSE and fraction incorrect, pooled across all pixel sizes, $p < 1 \times 10^{-10}$). However, the difference

in reconstruction quality between the optimal and empirical reconstructions was significantly larger in the raphe (Mann–Whitney U test; pooled across all pixel sizes, $p < 1 \times 10^{-10}$). These findings suggest that despite the fact that stimulation is less selective in the central retina (Fig. 5C,D), it is still sufficient to produce higher quality visual signals than in the peripheral retina.

Reconstruction of naturalistic images

The statistics of images in the natural visual world are very different from those of the white noise images tested above. To test how effectively the perception of naturalistic stimuli could be restored in the central retina using electrical stimulation, naturalistic images were reconstructed from evoked activity using a more sophisticated nonlinear reconstruction approach, as follows. Responses to flashed naturalistic images from the ImageNet database (Fei-Fei et al., 2009) were generated using the LNP model, and were used to compute optimal linear reconstruction filters. A convolutional autoencoder (CAE) was then trained to denoise the linear reconstructions generated from the filters (linear-CAE; see Materials and Methods; Parthasarathy et al., 2017). Using the same stimulation algorithm and procedure as above (Fig. 6; Shah et al., 2019b, 2022), expected reconstructions were then obtained from simulated electrically evoked responses, based on measured single-electrode stimulation data (Fig. 5), and were enhanced using the CAE. Several aspects of the naturalistic images (distinct shapes, textures, and high spatial frequency content) were more accurately captured by the raphe reconstructions than by the peripheral retina reconstructions (Fig. 7A), indicating that important features of naturalistic images can be restored in the raphe. The image quality (measured by NMSE and by SSIM, a perceptual similarity metric; Wang et al., 2004) was significantly higher in raphe preparations (Fig. 7B; Mann–Whitney U test; NMSE and SSIM, $p < 1 \times 10^{-10}$). In addition, similar to the white noise images (Fig. 6C), the error gap between the optimal and empirical naturalistic image reconstructions was significantly larger in raphe compared with peripheral preparations (Mann–Whitney U test; NMSE and SSIM, $p < 1 \times 10^{-10}$), highlighting the need for further improvement to the specificity of electrical stimulation in the central retina (see Discussion).

Estimation of midget cell activation

Although the majority of midget cells were not reliably identified in raphe recordings (Fig. 1A), electrical stimulation targeting parasol cells probably also activates many midget cells, because their activation thresholds are similar (Jepson et al., 2013; Madugula et al., 2022a). This inadvertent activation could introduce noise into any aspect of visual perception that is based on both parasol and midget cell signals. To estimate the extent of noise corruption, a raphe recording with partially complete ON and OFF midget cell populations (Fig. 8A) was used to simulate complete populations of ON and OFF midget cells, including their light and electrical stimulation response properties (Fig. 8B, C; see Materials and Methods). Then, using these properties (Fig. 8B,C) and the electrical stimulus sequence targeting parasol cells (Figs. 6, 7), the expected midget cell reconstruction was determined (see Materials and Methods) and summed with the expected parasol cell reconstruction to estimate the average performance of the reconstruction with added noise, for both white noise and naturalistic images. For the naturalistic image reconstructions, the same trained CAE used above (Fig. 7) was applied to denoise the reconstructions. In this simulation, the

recorded responses to electrical stimulation of midget cells were not used in optimizing electrical stimulation—a worst-case analysis.

Not surprisingly, inadvertent activation of midget cells added significant high-spatial frequency noise to both white noise and naturalistic image reconstructions (Fig. 8D–G). For white noise image reconstructions, to reduce the magnitude of the midget cell noise, a modification of the stimulation algorithm was implemented. Normally, the algorithm chooses electrical stimuli until no further reduction in expected MSE between the parasol cell reconstruction and the target image is possible (Shah et al., 2019b, 2022). However implementation of an early stopping criterion that takes into account an estimate of the midget cell noise (see Materials and Methods) resulted in a smaller number of electrical stimuli, strongly reducing the midget cell noise contribution (Fig. 8D,F), and thus increasing the quality of the final reconstructed image, although a significant noise corruption from midget cell activation still remained (6–56% increase in RMSE; 14–240% increase in fraction incorrect pixels; Fig. 8F). For naturalistic image reconstruction, application of the CAE to the linear parasol and midget cell reconstruction removed much of the high-spatial frequency noise contributed by midget cells, leaving only a small amount of noise in the final image (4% increase in RMSE and 1 - SSIM, Fig. 8E,G).

The fact that the parasol signal is still recognizable in the reconstructions (Fig. 8D,E) suggests that inadvertent midget cell activation, while significant, may not be a major problem, particularly when algorithmic modifications such as early stopping are implemented or when natural image priors are taken into account, as with the CAE (see Discussion). This analysis was repeated with a second raphe recording (data not shown), showing similar results, as follows: 1–13% increase in RMSE, 21–275% increase in the fraction of incorrect pixels for white noise images; and <1% increase in RMSE and 1 - SSIM for naturalistic images.
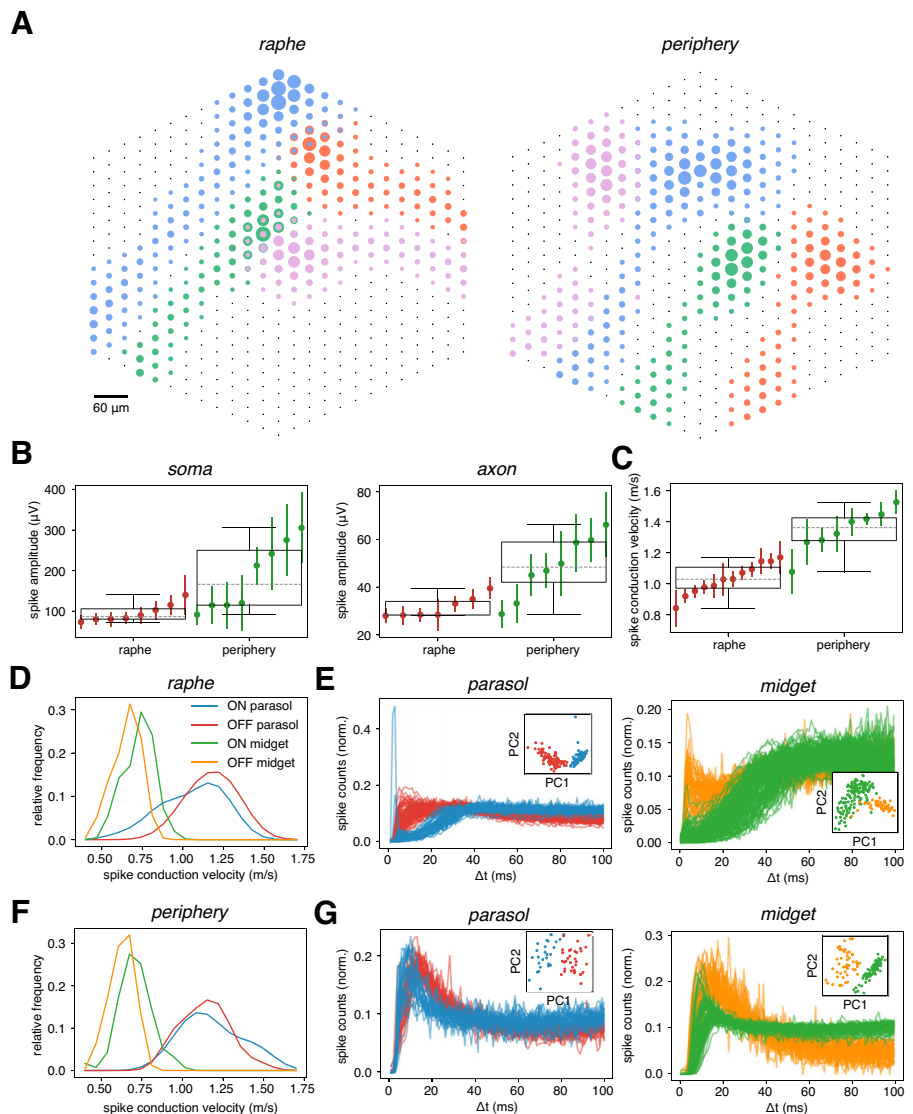
Figure 4. Electrical images and distinguishing cell types from intrinsic spiking and electrical features in the raphe. **A**, Example electrical images of four simultaneously recorded RGCs in a raphe and peripheral recording. The black points denote the locations of individual electrodes on the multielectrode array. The collection of dots of a single color denotes the electrical image of a single cell, with the size of each dot being proportional to the peak recorded voltage on that electrode during the spike of that cell. **B**, Maximum recorded spike amplitudes within somatic and axonal compartments within the electrical image of each parasol cell. Each data point denotes the median (± 1 median absolute deviation) value in a single preparation. **C**, Spike conduction velocities of parasol cells obtained from axonal electrodes on the electrical image (see Materials and Methods). Each data point denotes the median (± 1 median absolute deviation) value in a single preparation. In each box plot, the box denotes the interquartile range, the dashed gray line denotes the median value of all points in the plot, and the bottom and top whiskers denote the first quartile minus 1.5 times the interquartile range and the third quartile plus 1.5 times the interquartile range, respectively. **D**, Axon spike conduction velocities of ON parasol, OFF parasol, ON midget, and OFF midget cells in a single raphe preparation. For visual clarity, fitted kernel density estimates evaluated on the range of the spike conduction velocity histogram of each cell type are plotted. **E**, Spike train autocorrelation functions for ON and OFF parasol (left) and ON and OFF midget cells (right) in a single raphe preparation. Projections onto the first two principal components from PCA of the ON and OFF parasol (left) and ON and OFF midget cell (right) autocorrelation functions are shown as insets. Axon spike conduction velocity (**D**) and spike train autocorrelation functions (**E**) can together distinguish four of the five numerically dominant cell types. Note that a different raphe preparation was used to show separability using the spike train autocorrelation function. **F**, Same as **D** but in the peripheral retina. **G**. Same as **E** but in the peripheral retina. A single peripheral preparation was used to show separability with axon spike conduction velocity and spike train autocorrelation function.

Discussion

We examined the quality of visual signals that can be restored in the raphe region of the central macaque retina with epiretinal electrical stimulation. The functional organization and light response properties of major RGC types in the raphe

were similar to those of the peripheral retina (Figs. 1-3), with some notable differences, and the four numerically dominant cell types could be distinguished using their recorded electrical features alone (Fig. 4D). Despite less precise control over electrical activation in the raphe compared with the peripheral retina (Fig. 5C,D), the
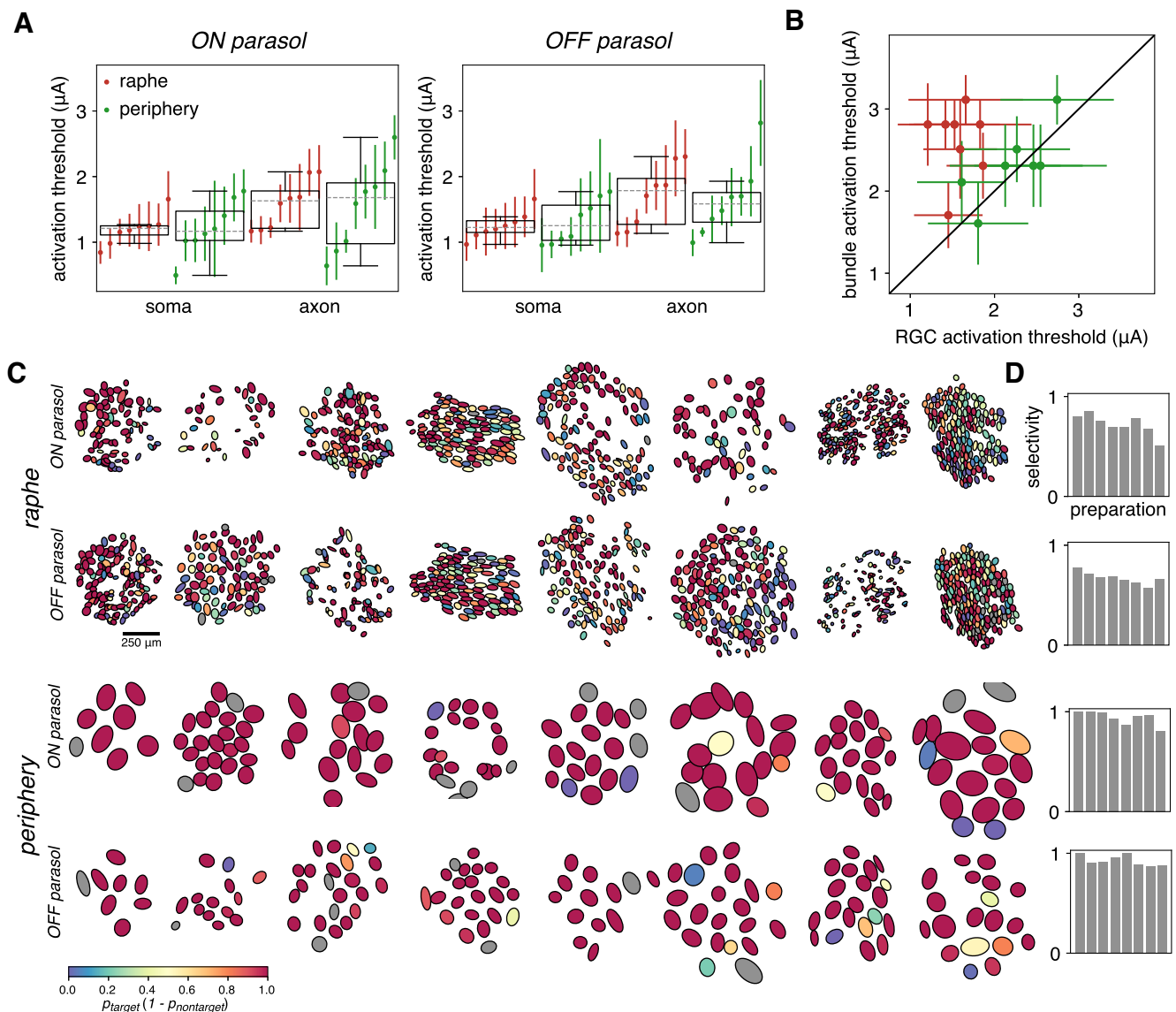
Figure 5. Electrical stimulation in the raphe and peripheral retina. *A*, Minimum somatic and axonal activation thresholds in ON parasol and OFF parasol cells. Each data point denotes the median (±1 median absolute deviation) value in a single preparation. *B*, Minimum activation threshold versus bundle activation threshold at each electrode. Each data point denotes the median (±1 median absolute deviation) value in a single preparation. *C*, ON parasol cell and OFF parasol cell RFs for eight raphe (top two rows) and eight peripheral retina (bottom two rows) preparations. The RF of each cell is colored according to its selectivity index (see Materials and Methods). RFs colored gray were excluded from electrical stimulation analysis because their evoked signals could not be distinguished from noise (see Materials and Methods). *D*, Average selectivity index values within each cell type and preparation.

unwanted activation of axons was lower in the raphe (Fig. 5B), and the estimated quality of restored visual signals in parasol cells was higher (Fig. 6A), over a range of spatial scales (Fig. 6B), and with naturalistic images (Fig. 7). These findings support the viability of targeting the raphe area for vision restoration with a high-fidelity epiretinal implant.

Image reconstruction with parasol cell signals in the raphe
The differences in visual reconstruction from electrically evoked signals in the raphe and periphery could not have been easily predicted on first principles alone, and thus required direct measurement. In particular, despite reduced stimulation selectivity (Fig. 5C,D), the fidelity of visual reconstruction was higher in the raphe (Figs. 6, 7), because of the greater reconstruction resolution afforded by more cells per unit area and because of the reduced activation of axon bundles. However, the difference in

performance between the optimal and empirical reconstructions was systematically larger in raphe preparations for white noise (Fig. 6) and naturalistic (Fig. 7) images, reflecting the reduced selectivity of stimulation relative to the peripheral retina (Fig. 5C,D).

Most raphe preparations exhibited higher-quality reconstructions with naturalistic images compared with peripheral preparations (Fig. 7). However, one raphe preparation in particular exhibited substantially lower performance (measured by NMSE) compared with other preparations (Fig. 7B), approaching the quality of some of the peripheral preparations. This is likely because of the poor selectivity of stimulation in this preparation (Fig. 5C, rightmost raphe preparation). Multielectrode stimulation strategies (Townshend and White, 1987; Sweeney et al., 1990; Bonham and Litvak, 2008; Martens et al., 2011) can be used to augment single-electrode stimulation, which may potentially enhance reconstruction performance. These methods
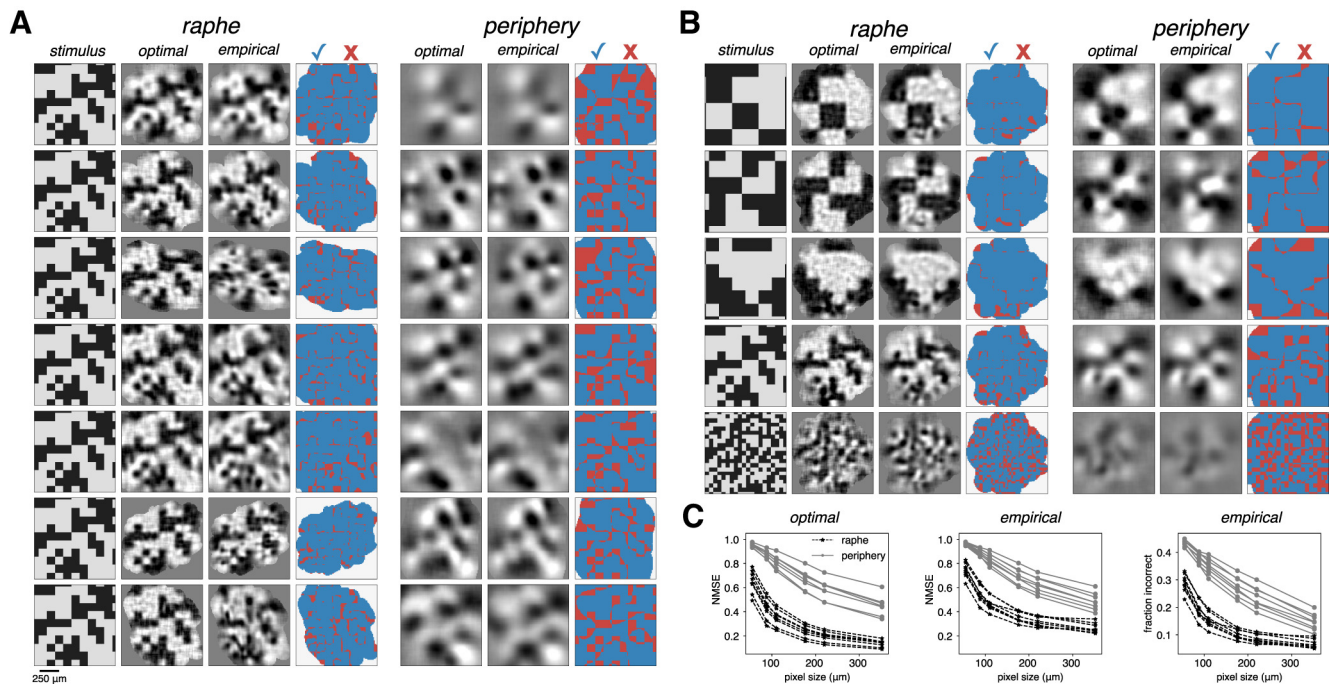
Figure 6. Inference of visual perception in the raphe and peripheral retina with white noise. **A,** Example linear reconstruction based on evoked RGC responses in individual raphe and peripheral preparations for a single white noise image (pixel size, 110 μm). Each row is a distinct retinal preparation for each retinal location (two preparations per row). The first column shows the original image; the second column shows the optimal reconstruction (i.e., that achievable with perfect control over the firing of each RGC); the third column shows the reconstruction that is achievable by optimized stimulation based on recorded evoked responses (Shah et al., 2019b, 2022; see Materials and Methods); the fourth column shows the pixels that were incorrectly reconstructed relative to the original image (red, incorrect; blue, correct). Columns 5–7 show the same as columns 2–4, but in the peripheral retina. **B,** Reconstruction of white noise images with different pixel sizes (352, 220, 176, 110, and 55 μm) in an example raphe and peripheral preparation. Each row is for a distinct white noise image. Columns show the same as in **A. C,** NMSE (the squared error normalized by L2-norm of target image squared) in the optimal reconstructions (left), the empirical reconstructions (middle), and the fraction of incorrectly reconstructed pixels in the empirical reconstructions (right). Each data point denotes the average of 15 images at each pixel size examined for a single preparation.

have been applied previously in the peripheral retina for minimizing inadvertent neighboring RGC activation (Jepson et al., 2014a; Fan et al., 2019) as well as distant RGC activation (Nanduri, 2011) by the active avoidance of axonal stimulation (Vilkhu et al., 2021), using biophysical models of cellular activation as a theoretical basis (Rattay, 1986, 1999; Rattay and Resatz, 2004).

Contribution of midget cell signals
Although analysis of ON and OFF parasol cells (Figs. 5–7) provides an indication of the visual image that can be encoded by electrical stimulation, it is not a complete representation of the visual neural code. Parasol cells constitute ~15% of the overall RGC input to the brain (Dacey, 2004) and a lower percentage in the central retina (Marshak, 2009). Midget cells (~50%) mediate high-acuity vision in primates, and color vision is thought to be mediated primarily by midget and small bistratified (~5%) cells (Dacey, 2004; Field et al., 2007, 2010). Most midget and small bistratified cell spikes were not reliably identified in the raphe recordings (Fig. 1A), so their exact impact on reconstruction could not be measured. Instead, a data-driven simulation of inadvertently evoked midget cell responses to electrical stimulation when targeting the parasol cells was used to reveal a high-spatial frequency noise component that increases the error (Fig. 8D–G). However, particularly when an early stopping criterion was implemented for white noise images (Fig. 8D,F) or when natural image priors were imposed for naturalistic images (Fig. 8E,G), much of the reconstruction from parasol cell signals was still recognizable, suggesting that unwanted midget cell activation may not be a severe problem. Nevertheless, improved spike sorting for reliably

identifying spikes from all cell types, particularly the very numerous midget cells, is an important direction for future work.

The density of peripheral midget cells is comparable to that of raphe parasol cells (Fig. 1). Thus, with respect to spatial resolution, it may be that targeting central parasol cells provides a visual signal of comparable resolution to that from targeting peripheral midget cells. However, there are at least two other considerations. First, it may be that targeting the central retina, which a normally sighted individual uses to scan the scene with eye movements, is intrinsically important for perception. Second, midget cells could potentially subserve a different kind of perceptual experience than parasol cells. Although it is not presently clear whether peripheral midget or central parasol cells are more useful for vision restoration, future *in vivo* work in primates could be used to target the raphe parasol and peripheral midget cells separately and independently to fully understand their respective contributions to perception.

Light response properties of raphe RGCs
Relatively little is known about differences in light response properties and intrinsic electrical properties between central and peripheral RGCs. Previous *in vivo* studies in the macaque retina have examined several chromatic, spatial, and temporal response properties in parafoveal and central RGCs (Lee et al., 1989a, b, 1990; Passaglia et al., 2002). In particular, differences in responses to stimuli of varying temporal frequencies were reported between central and peripheral RGCs (Lee et al., 1990; Solomon et al., 2002). A more recent *ex vivo* study of macaque RGCs (Sinha et al., 2017) directly compared differences in response kinetics between central and peripheral RGCs and
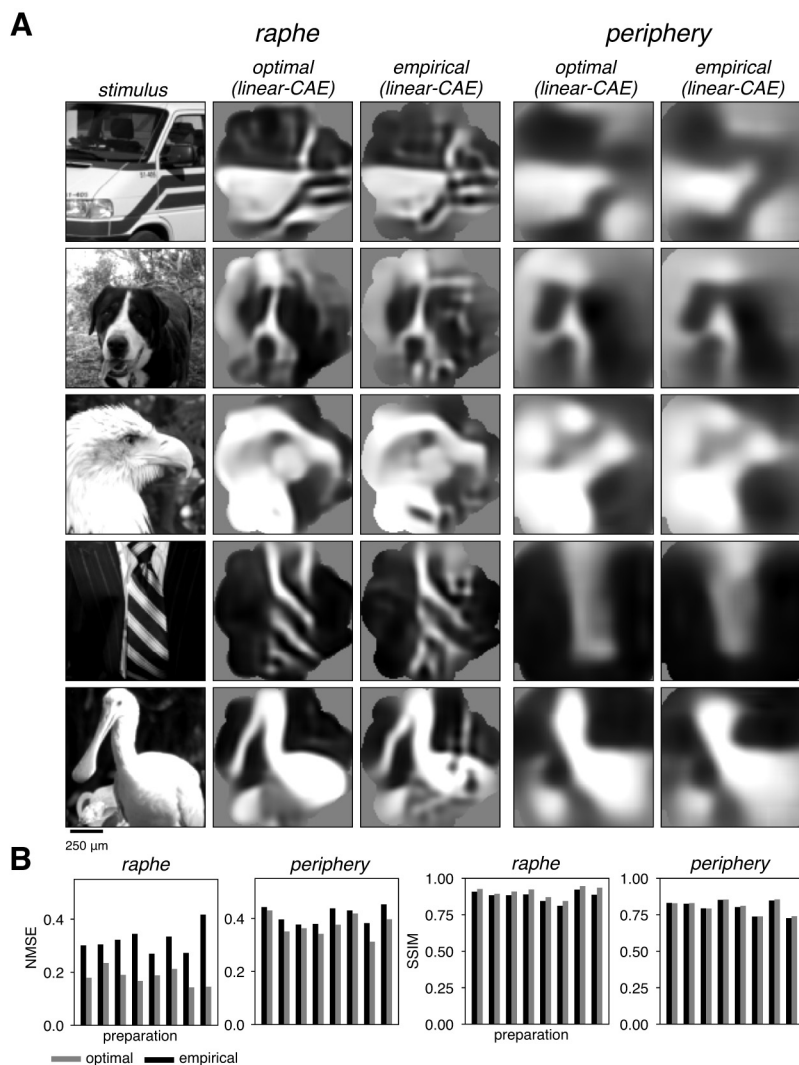
Figure 7. Inference of visual perception in the raphe and peripheral retina with naturalistic images. *A*, Reconstruction of naturalistic images from the ImageNet database (Fei-Fei et al., 2009) in an example raphe (left) and peripheral (right) preparation after image enhancement with a CAE (Parthasarathy et al., 2017; see Materials and Methods). Each row corresponds to a distinct image. The first column shows the original image; the second column shows the optimal reconstruction (i.e., achievable with perfect control over the firing of each RGC); the third column shows the reconstruction that is achievable by optimized stimulation (Shah et al., 2019b, 2022; see Materials and Methods). Columns 4 and 5 are the same as columns 2 and 3, but for an example peripheral preparation. Scale bar, 250 μm (visual angle, 1.25°). *B*, Optimal and empirical NMSE (squared error normalized by L2-norm of target image squared; left) and SSIM (right; Wang et al., 2004) averaged over 100 naturalistic images from the ImageNet database for each raphe and peripheral preparation. Note that in some of the peripheral preparations, the average SSIM for the empirical reconstructions is slightly higher than for the optimal reconstructions, which is possible because the CAE is trained to minimize MSE (see Materials and Methods).

reported that central cells have slower light responses, likely as a result of differences in cone photoreceptor kinetics. While the overall functional organization and light response properties appear to be similar in the central and peripheral retina (Figs. 1, 2), the differences observed here build on prior work and reveal ON–OFF asymmetries—namely, slower response kinetics and a more nonlinear contrast response in OFF versus ON cells—as well as how they compare to the asymmetries in the peripheral retina (Fig. 2E,F; Chichilnisky and Kalmar, 2002).

Spiking and electrical properties of raphe RGCs

The precise origin of differences in doublet firing tendency in ON parasol cells and spike rate in OFF parasol cells between raphe and peripheral RGCs (Fig. 3A,B) is uncertain. Although it is possible that central versus peripheral parasol cells have differences in intrinsic excitability, differences in response kinetics and contrast response (Fig. 2E,F) could produce differences in spiking statistics during visual stimulation. Future work could more thoroughly probe the origin by analyzing spontaneous activity. Differences in the width of cross-correlations (Fig. 3C,D) between homotypic nearest-neighbor central and peripheral parasol cells are likely because of response time course differences (Fig. 2E): there was a positive correlation between the width of cross-correlations and the time of zero crossing in the time course across preparations (data not shown). Future work could analyze spontaneous recordings or responses to repeated white noise stimuli (Trong and Rieke, 2008; Greschner et al., 2011) to better understand circuit-level versus stimulus-driven components of correlated firing.

Spike amplitude differences between raphe and peripheral parasol cells (Fig. 4B) may reflect differences in the sizes of both somatic and axonal compartments (Bestel et al., 2017), which increase with eccentricity (Rodieck et al., 1985; Sanchez et al., 1986; Watanabe and Rodieck, 1989; Walsh et al., 2000; FitzGibbon and Taylor, 2012). The smaller axon diameters also may contribute to the slower axon spike conduction velocities in raphe parasol cells (Fig. 4C; Hodgkin, 1954), as has been demonstrated previously in the primate and cat retina (Hsiao et al., 1984; Fukuda et al., 1988).

Spiking statistics and electrical properties were sufficient to distinguish ON and OFF parasol and midget cells in the raphe (Fig. 4D,E), as has been demonstrated previously in the peripheral retina (Fig. 4F,G; Richard et al., 2016; Madugula et al., 2022a; Zaidi et al., 2022). However, it is unclear how effective this method will be in a degenerated retina. Previous work in rat models of photoreceptor degeneration reported altered sodium and potassium channel expression in RGCs (Chen et al., 2013), which may affect spike conduction velocity, potentially diminishing the ability to distinguish parasol from midget cells. However, a prior investigation revealed that cell type differences in spike waveforms were preserved during photoreceptor degeneration in rats (Yu et al., 2017), suggesting that electrical properties, and potentially spike conduction velocity, can still be leveraged to separate distinct cell types during degeneration. In addition, previous studies have shown differences in intrinsic RGC excitability between healthy and degenerated rat retinas (Sekirnjak et al., 2011; Ren et al., 2018). Although it was reported that differences in spiking statistics between ON and OFF cells in the rat retina increased during degeneration (Sekirnjak et al., 2011), implying increased ability to distinguish OFF cells from ON, it is unknown whether this will apply to the primate retina or to specific cell types within the broad ON and OFF categories.

Finally, several technical limitations of this study could be addressed in future work.
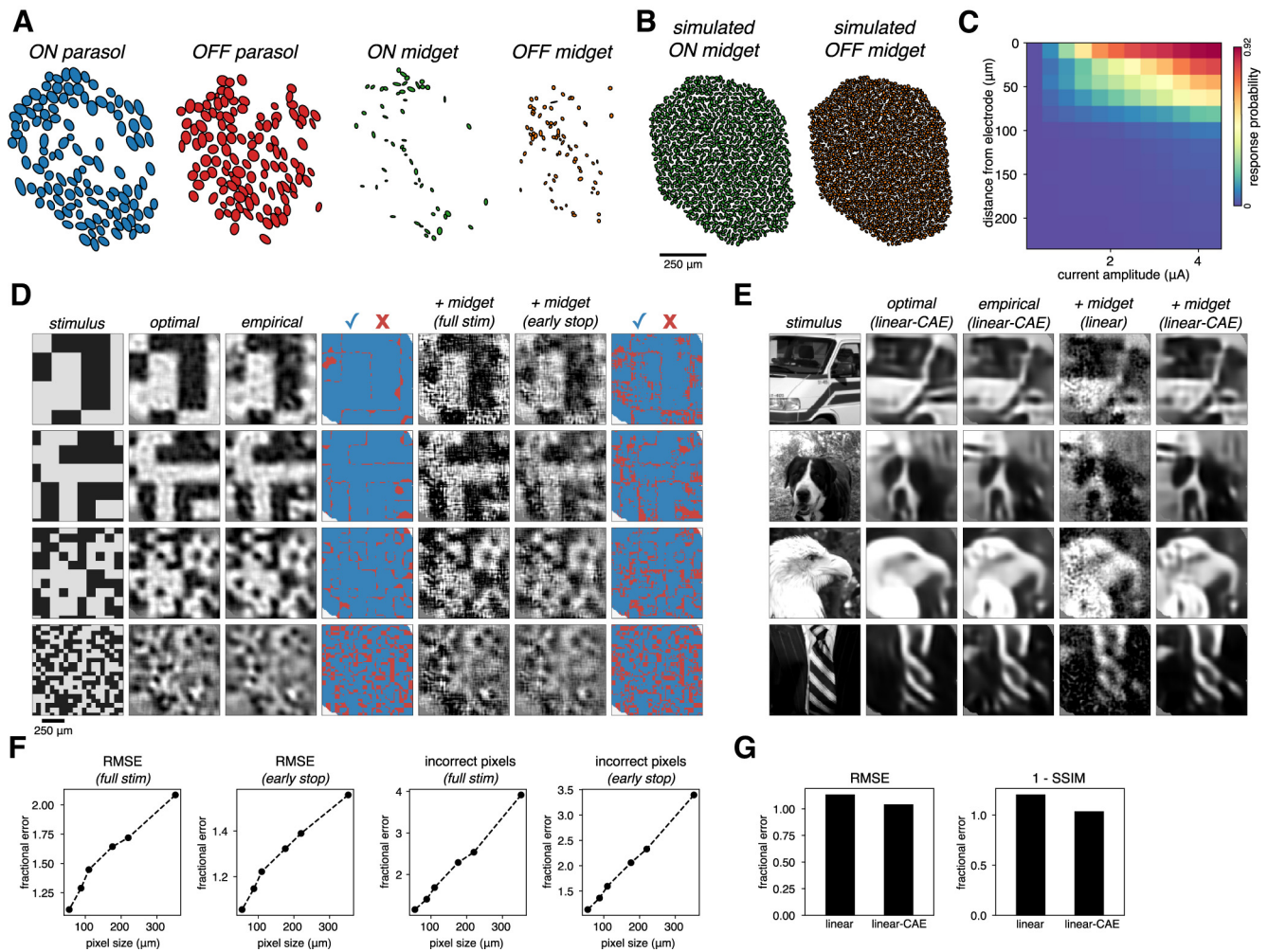
Figure 8. Estimation of midget cell activation. ***A***, Receptive fields (2σ boundary from a Gaussian fit to the spatial component of the STA) of nearly complete ON parasol and OFF parasol cell populations and partial ON midget and OFF midget cell populations, in a single raphe preparation. ***B***, Receptive fields of simulated complete populations of ON midget and OFF midget cells in the same preparation as ***A*** (see Materials and Methods). ***C***, Response probability as a function of distance from stimulating electrode and applied current (see Materials and Methods). This relationship was determined using all of the electrical stimuli and responses from recorded midget cells in ***A***. ***D***, White noise reconstructions from parasol cells and the resulting reconstruction from the activation of simulated midget cells, in a single raphe preparation (***A–C***; pixel sizes shown, 352, 220, 110, and 55 µm). The first column shows the original image; the second column shows the optimal reconstruction (i.e., achievable with perfect control over the firing of each RGC); the third column shows the empirical reconstruction that is achievable by optimized stimulation based on recorded evoked responses (Shah et al., 2019b, 2022; see Materials and Methods); the fourth column shows the pixels that were incorrectly reconstructed relative to the original image (red, incorrect; blue, correct); the fifth column shows the reconstruction (third column) summed with the simulated midget cell noise (see Materials and Methods); the sixth column shows the reconstruction summed with the simulated midget cell noise that can be achieved using an early stopping criterion (see Materials and Methods); the seventh column shows the pixels that were incorrectly reconstructed relative to the original image using the early stopping criterion (red, incorrect; blue, correct). ***E***, Naturalistic image reconstructions from parasol cells and the resulting reconstruction from the activation of midget cells in the same preparation as ***D***. The first column shows the original image; the second column shows the optimal reconstruction after application of the same trained CAE as in Figure 7; the third column shows the empirical reconstruction after application of the CAE; the fourth column shows the linear empirical parasol cell reconstruction (linear portion of column 3) summed with the linear simulated midget cell noise; the fifth column shows the resulting image after applying the CAE to the image in column 4. ***F***, Fractional error (see Materials and Methods) between the white noise empirical parasol cell reconstruction (column D3) and the empirical parasol cell reconstruction summed with midget cell noise, after full stimulation (column D5) or after early stopping (column D6). Each data point denotes the average fractional error over 15 images at each pixel size. ***G***, Fractional error between the naturalistic image empirical parasol cell reconstruction and the empirical parasol cell reconstruction summed with the midget cell noise. Fractional error was calculated using both the linear reconstructions as well as the linear reconstructions enhanced by the CAE (see Materials and Methods). The bar plots denote the average fractional error over 100 naturalistic images.

1. White noise visual stimulation for light response modeling (Fig. 2) is limited because its statistics differ greatly from the statistics of naturalistic stimuli, and could elicit RGC responses that are much different from what would be observed in natural viewing conditions (Heitman et al., 2016). Thus, future work could focus on performing naturalistic image stimulation for response modeling in the central retina (Heitman et al., 2016; McIntosh et al., 2016), which may require models that take into account additional properties such as cell–cell interactions (Mastronarde, 1983; Pillow et al., 2008) and spatial nonlinearities (Hochstein and Shapley, 1976; Shah et al., 2020).

2. Pixel-wise MSE, although a standard and intuitive objective function to minimize loss between target and reconstructed images, does not fully capture the quality of image reconstruction relevant for vision (Wandell, 1995). Future work could optimize the perceptual similarity of reconstructed images (Shah et al., 2019b, 2022) using metrics such as SSIM (Wang et al., 2004; Parthasarathy et al., 2017; Wu et al., 2022).

3. Linear reconstruction (Warland et al., 1997; Brackbill et al., 2020), although simple and computationally tractable, is likely too simple an approximation for how the visual system extracts information from RGC spike trains to produce visual perception and behaviors. Future work could apply more sophisticated nonlinear reconstruction methods for optimizing visual perception (Parthasarathy et al., 2017; Zhang et al., 2020; Kim et al., 2021; Wu et al., 2022), such as the CAE used to enhance the naturalistic image reconstructions here (Parthasarathy et al., 2017; Fig. 7, 8E) or denoisers trained on naturalistic images (Wu et al., 2022).

4. In each reconstruction analysis, the expected value of the parasol cell reconstruction (Figs. 6, 7) and simulated midget cell noise contribution (Fig. 8) were analyzed. A single trial of the parasol reconstruction resulting from the stimulation algorithm is similar to the expected value because of the variance penalty used in optimization (Shah et al., 2019b, 2022). However, a single trial of the simulated midget cell noise tends to be larger in magnitude than the expected value (data not shown) because there is no regularization possible when considering responses *post hoc*. Future work could include modifications to the stimulation algorithm to minimize reconstruction error introduced by inadvertent midget cell stimulation on a single trial.

5. Several assumptions were made about how parasol and midget cell signals and natural image priors are combined to produce reconstructions. Reconstruction filters for parasol and simulated midget cells were learned separately. However, previous work has demonstrated that the cell types included when learning filters using least-squares regression strongly influence the features of the filter of any given cell (Brackbill et al., 2020). Indeed, when the parasol and simulated midget cell filters were learned together, the strength of the parasol cell filters was suppressed substantially relative to that of the simulated midget cells compared with when the filters were learned separately (data not shown). Also, the CAE was trained only on linear reconstructions obtained from parasol cells (Fig. 8E,G). When the CAE was instead trained on parasol and simulated midget cell signals together, the fidelity of the denoised parasol cell reconstruction with added midget cell noise was lower (data not shown). Future work could further explore how the relative weighting of signals from different cell types and image priors influences image reconstruction.

References

Bestel R, Appali R, van Rienen U, Thielemann C (2017) Effect of morphologic features of neurons on the extracellular electric potential: a simulation study using cable theory and electro-quasi-static equations. Neural Comput 29:2955–2978.

Bonham BH, Litvak LM (2008) Current focusing and steering: modeling, physiology, and psychophysics. Hear Res 242:141–153.

Brackbill N, Rhoades C, Kling A, Shah NP, Sher A, Litke AM, Chichilnisky EJ (2020) Reconstruction of natural images from responses of primate retinal ganglion cells. Elife 9:e58516.

Chen Z, Song Y, Yao J, Weng C, Yin ZQ (2013) Alterations of sodium and potassium channels of RGCs in RCS rat with the development of retinal degeneration. J Mol Neurosci 51:976–985.

Chichilnisky EJ (2001) A simple white noise analysis of neuronal light responses. Network 12:199–213.

Chichilnisky EJ, Kalmar RS (2002) Functional asymmetries in ON and OFF ganglion cells of primate retina. J Neurosci 22:2737–2747.

Dacey DM (2004) Origins of perception: retinal ganglion cell diversity and the creation of parallel visual pathways. In: The cognitive neurosciences (Gazzaniga MS, ed), pp 281–301. Cambridge, MA: MIT.

Dacey DM, Petersen MR (1992) Dendritic field size and morphology of midget and parasol ganglion cells of the human retina. Proc Natl Acad Sci U S A 89:9666–9670.

Fan VH, Grosberg LE, Madugula SS, Hottowy P, Dabrowski W, Sher A, Litke AM, Chichilnisky EJ (2019) Epiretinal stimulation with local returns enhances selectivity at cellular resolution. J Neural Eng 16:025001.

Fei-Fei L, Deng J, Li K (2009) ImageNet: constructing a large-scale image database. J Vis 9:1037.

Field GD, Sher A, Gauthier JL, Greschner M, Shlens J, Litke AM, Chichilnisky EJ (2007) Spatial properties and functional organization of small bistratified ganglion cells in primate retina. J Neurosci 27:13261–13272.

Field GD, Gauthier JL, Sher A, Greschner M, Machado TA, Jepson LH, Shlens J, Gunning DE, Mathieson K, Dabrowski W, Paninski L, Litke AM, Chichilnisky EJ (2010) Functional connectivity in the retina at the resolution of photoreceptors. Nature 467:673–677.

FitzGibbon T, Taylor SF (2012) Mean retinal ganglion cell axon diameter varies with location in the human retina. Jpn J Ophthalmol 56:631–637.

Fukuda Y, Watanabe M, Wakakuwa K, Sawai H, Morigiwa K (1988) Intraretinal axons of ganglion cells in the Japanese monkey (Macaca fuscata): conduction velocity and diameter distribution. Neurosci Res 6:53–71.

Gauthier JL, Field GD, Sher A, Greschner M, Shlens J, Litke AM, Chichilnisky EJ (2009a) Receptive fields in primate retina are coordinated to sample visual space more uniformly. PLoS Biol 7:e1000063.

Gauthier JL, Field GD, Sher A, Shlens J, Greschner M, Litke AM, Chichilnisky EJ (2009b) Uniform signal redundancy of parasol and midget ganglion cells in primate retina. J Neurosci 29:4675–4680.

Goetz GA, Palanker DV (2016) Electronic approaches to restoration of sight. Rep Prog Phys 79:096701.

Greschner M, Shlens J, Bakolitsa C, Field GD, Gauthier JL, Jepson LH, Sher A, Litke AM, Chichilnisky EJ (2011) Correlated firing among major ganglion cell types in primate retina. J Physiol 589:75–86.

Grosberg LE, Ganesan K, Goetz GA, Madugula SS, Bhaskhar N, Fan V, Li P, Hottowy P, Dabrowski W, Sher A, Litke AM, Mitra S, Chichilnisky EJ (2017) Activation of ganglion cells and axon bundles using epiretinal electrical stimulation. J Neurophysiol 118:1457–1471.

Heitman A, Brackbill N, Greschner M, Sher A, Litke AM, Chichilnisky EJ (2016) Testing pseudo-linear models of responses to natural scenes in primate retina. bioRxiv 045336. https://doi.org/10.1101/045336.

Hochstein S, Shapley RM (1976) Linear and nonlinear spatial subunits in Y cat retinal ganglion cells. J Physiol 262:265–284.

Hodgkin AL (1954) A note on conduction velocity. J Physiol 125:221–224.

Hottowy P, Dąbrowski W, Skoczeń A, Wiącek P (2008) An integrated multichannel waveform generator for large-scale spatio-temporal stimulation of neural tissue. Analog Integr Circ Sig Process 55:239–248.

Hottowy P, Skoczeń A, Gunning DE, Kachiguine S, Mathieson K, Sher A, Wiącek P, Litke AM, Dąbrowski W (2012) Properties and application of a multichannel integrated circuit for low-artifact, patterned electrical stimulation of neural tissue. J Neural Eng 9:066005.

Hsiao C-F, Watanabe M, Fukuda Y (1984) The relation between axon diameter and axonal conduction velocity of Y, X and W cells in the cat retina. Brain Res 309:354–356.

Jepson LH, Hottowy P, Mathieson K, Gunning DE, Dabrowski W, Litke AM, Chichilnisky EJ (2013) Focal electrical stimulation of major ganglion cell types in the primate retina for the design of visual prostheses. J Neurosci 33:7194–7205.

Jepson LH, Hottowy P, Mathieson K, Gunning DE, Dąbrowski W, Litke AM, Chichilnisky EJ (2014a) Spatially patterned electrical stimulation to enhance resolution of retinal prostheses. J Neurosci 34:4871–4881.

Jepson LH, Hottowy P, Weiner GA, Dabrowski W, Litke AM, Chichilnisky EJ (2014b) High-fidelity reproduction of spatiotemporal visual signals for retinal prosthesis. Neuron 83:87–92.

Kim YJ, Brackbill N, Batty E, Lee J, Mitelut C, Tong W, Chichilnisky EJ, Paninski L (2021) Nonlinear decoding of natural images from large-scale primate retinal ganglion recordings. Neural Comput 33:1719–1750.

Kingma DP, Ba J (2014) Adam: a method for stochastic optimization. arXiv. Advance online publication. Retrieved May 15, 2023.

Lee BB, Martin PR, Valberg A (1989a) Sensitivity of macaque retinal ganglion cells to chromatic and luminance flicker. J Physiol 414:223–243.

Lee BB, Martin PR, Valberg A (1989b) Amplitude and phase of responses of macaque retinal ganglion cells to flickering stimuli. J Physiol 414:245–263.

Lee BB, Pokorny J, Smith VC, Martin PR, Valberg A (1990) Luminance and chromatic modulation sensitivity of macaque ganglion cells and human observers. J Opt Soc Am A 7:2223–2236.

Li PH, Gauthier JL, Schiff M, Sher A, Ahn D, Field GD, Greschner M, Callaway EM, Litke AM, Chichilnisky EJ (2015) Anatomical identification of extracellularly recorded cells in large-scale multielectrode recordings. J Neurosci 35:4663–4675.

Litke AM, Bezayiff N, Chichilnisky EJ, Cunningham W, Dabrowski W, Grillo AA, Grivich M, Grybos P, Hottowy P, Kachiguine S, Kalmar RS, Mathieson K, Petrusca D, Rahman M, Sher A (2004) What does the eye tell the brain? Development of a system for the large-scale recording of retinal output activity. IEEE Trans Nucl Sci 51:1434–1440.

Madugula SS, Gogliettino AR, Zaidi M, Aggarwal G, Kling A, Shah NP, Brown JB, Vilkhu R, Hays MR, Nguyen H, Fan V, Wu EG, Hottowy P, Sher A, Litke AM, Silva RA, Chichilnisky EJ (2022a) Focal electrical stimulation of human retinal ganglion cells for vision restoration. J Neural Eng 19:066040.

Madugula SS, Vilkhu R, Shah NP, Grosberg LE, Kling A, Gogliettino AR, Nguyen H, Hottowy P, Sher A, Litke AM, Chichilnisky EJ (2022b) Inference of electrical stimulation sensitivity from recorded activity of primate retinal ganglion cells. bioRxiv 465478. https://doi.org/10.1101/2021.10.22.465478.

Marshak DW (2009) Retinal ganglion cells: anatomy. In: Encyclopedia of neuroscience (Squire L, ed), pp 211–218. Amsterdam: Elsevier.

Martens HCF, Toader E, Decré MMJ, Anderson DJ, Vetter R, Kipke DR, Baker KB, Johnson MD, Vitek JL (2011) Spatial steering of deep brain stimulation volumes using a novel lead design. Clin Neurophysiol 122:558–566.

Mastronarde DN (1983) Correlated firing of cat retinal ganglion cells. I. Spontaneously active inputs to X- and Y-cells. J Neurophysiol 49:303–324.

McIntosh LT, Maheswaranathan N, Nayebi A, Ganguli S, Baccus SA (2016) Deep learning models of the retinal response to natural scenes. Adv Neural Inf Process Syst 29:1369–1377.

Meister M, Berry MJ 2nd (1999) The neural code of the retina. Neuron 22:435–450.

Müller J, Ballini M, Livi P, Chen Y, Radivojevic M, Shadmani A, Viswam V, Jones IL, Fiscella M, Diggelmann R, Stettler A, Frey U, Bakkum DJ, Hierlemann A (2015) High-resolution CMOS MEA platform to study neurons at subcellular, cellular, and network levels. Lab Chip 15:2767–2780.

Nanduri D (2011) Prosthetic vision in blind human patients: predicting the percepts of epiretinal stimulation. PhD thesis, University of Southern California.

Pachitariu M, Steinmetz N, Kadir S, Carandini M, Harris K (2016) Fast and accurate spike sorting of high-channel count probes with KiloSort. In: Proceedings of 30th Conference on Neural Information Processing Systems (NIPS 2016) (Lee D, Sugiyama M, Luxburg U, Guyon I, Garnett R), pp 4448–4456. San Diego, CA: Neural Information Processing Systems Foundation.

Parthasarathy N, Batty E, Falcon W, Rutten T, Rajpal M, Chichilnisky EJ, Paninski L (2017) Neural networks for efficient Bayesian decoding of natural images from retinal neurons. In: Advances in neural information processing systems: 31st Conference on Neural Information Processing Systems (NIPS 2017) (Guyon I, Luxburg UV, Bengio S, Wallach H, Fergus R, Vishwanathan S, Garnett R, eds), pp 6434–6445. Red Hook, NY: Curran Associates.

Passaglia CL, Troy JB, Rüttiger L, Lee BB (2002) Orientation sensitivity of ganglion cells in primate retina. Vision Res 42:683–694.

Petrusca D, Grivich MI, Sher A, Field GD, Gauthier JL, Greschner M, Shlens J, Chichilnisky EJ, Litke AM (2007) Identification and characterization of a Y-like primate retinal ganglion cell type. J Neurosci 27:11019–11027.

Pillow JW, Shlens J, Paninski L, Sher A, Litke AM, Chichilnisky EJ, Simoncelli EP (2008) Spatio-temporal correlations and visual signalling in a complete neuronal population. Nature 454:995–999.

Rattay F (1986) Analysis of models for external stimulation of axons. IEEE Trans Biomed Eng 33:974–977.

Rattay F (1999) The basic mechanism for the electrical stimulation of the nervous system. Neuroscience 89:335–346.

Rattay F, Resatz S (2004) Effective electrode configuration for selective stimulation with inner eye prostheses. IEEE Trans Biomed Eng 51:1659–1664.

Ren Y-M, Weng C-H, Zhao C-J, Yin Z-Q (2018) Changes in intrinsic excitability of ganglion cells in degenerated retinas of RCS rats. Int J Ophthalmol 11:756–765.

Rhoades CE, Shah NP, Manookin MB, Brackbill N, Kling A, Goetz G, Sher A, Litke AM, Chichilnisky EJ (2019) Unusual physiological properties of smooth monostratified ganglion cell types in primate retina. Neuron 103:658–672.e6.

Richard E, Goetz GA, Chichilnisky EJ (2016) Recognizing retinal ganglion cells in the dark. Adv Neural Inf Process Syst 28:2467–2475.

Rodieck RW (1965) Quantitative analysis of cat retinal ganglion cell response to visual stimuli. Vision Res 5:583–601.

Rodieck RW, Binmoeller KF, Dineen J (1985) Parasol and midget ganglion cells of the human retina. J Comp Neurol 233:115–132.

Roska B, Meister M (2013) The retina dissects the visual scene. In: The new visual neurosciences (Werner JS, Chalupa JM, eds), pp 163–182, Chap 13. Cambridge, MA: MIT.

Sanchez RM, Dunkelberger GR, Quigley HA (1986) The number and diameter distribution of axons in the monkey optic nerve. Invest Ophthalmol Vis Sci 27:1342–1350.

Sekirnjak C, Hottowy P, Sher A, Dabrowski W, Litke AM, Chichilnisky EJ (2006) Electrical stimulation of mammalian retinal ganglion cells with multielectrode arrays. J Neurophysiol 95:3311–3327.

Sekirnjak C, Hottowy P, Sher A, Dabrowski W, Litke AM, Chichilnisky EJ (2008) High-resolution electrical stimulation of primate retina for epiretinal implant design. J Neurosci 28:4446–4456.

Sekirnjak C, Jepson LH, Hottowy P, Sher A, Dabrowski W, Litke AM, Chichilnisky EJ (2011) Changes in physiological properties of rat ganglion cells during retinal degeneration. J Neurophysiol 105:2560–2571.

Shah N, Madugula S, Hottowy P, Sher A, Litke A, Paninski L, Chichilnisky EJ (2019a) Efficient characterization of electrically evoked responses for neural interfaces. Adv Neural Inf Process Syst 32:14444–14458.

Shah NP, Madugula S, Grosberg L, Mena G, Tandon P, Hottowy P, Sher A, Litke A, Mitra S, Chichilnisky EJ (2019b) Optimization of electrical stimulation for a high-fidelity artificial retina. In: 2019 9th international IEEE/EMBS conference on neural engineering (NER), pp 714–718. Piscataway, NJ: IEEE.

Shah NP, Brackbill N, Rhoades C, Kling A, Goetz G, Litke AM, Sher A, Simoncelli EP, Chichilnisky EJ (2020) Inference of nonlinear receptive field subunits with spike-triggered clustering. Elife 9:e45743.

Shah NP, Madugula S, Phillips AJ, Grosberg L, Gogliettino AR, Dusi A, Tandon P, Brown J, Hottowy P, Dabrowski W, Sher A, Litke AM, Mitra S, Chichilnisky EJ (2022) Precise control of neural activity using temporally dithered and spatially multiplexed electrical stimulation. bioRxiv 501643. https://doi.org/10.1101/2022.07.26.501643.

Shlens J, Field GD, Gauthier JL, Grivich MI, Petrusca D, Sher A, Litke AM, Chichilnisky EJ (2006) The structure of multi-neuron firing patterns in primate retina. J Neurosci 26:8254–8266.

Shlens J, Field GD, Gauthier JL, Greschner M, Sher A, Litke AM, Chichilnisky EJ (2009) The structure of large-scale synchronized firing in primate retina. J Neurosci 29:5022–5031.

Sinha R, Hoon M, Baudin J, Okawa H, Wong ROL, Rieke F (2017) Cellular and circuit mechanisms shaping the perceptual properties of the primate fovea. Cell 168:413–426.e12.

Solomon SG, Martin PR, White AJR, Rüttiger L, Lee BB (2002) Modulation sensitivity of ganglion cells in peripheral retina of macaque. Vision Res 42:2893–2898.

Sweeney JD, Ksienski DA, Mortimer JT (1990) A nerve cuff technique for selective excitation of peripheral nerve trunk regions. IEEE Trans Biomed Eng 37:706–715.

Tandon P, Bhaskhar N, Shah N, Madugula S, Grosberg L, Fan VH, Hottowy P, Sher A, Litke AM, Chichilnisky EJ, Mitra S (2021) Automatic identification of axon bundle activation for epiretinal prosthesis. IEEE Trans Neural Syst Rehabil Eng 29:2496–2502.

Townshend B, White RL (1987) Reduction of electrical interaction in auditory prostheses. IEEE Trans Biomed Eng 34:891–897.

Trong PK, Rieke F (2008) Origin of correlated activity between parasol retinal ganglion cells. Nat Neurosci 11:1343–1351.

Vilkhu RS, Madugula SS, Grosberg LE, Gogliettino AR, Hottowy P, Dabrowski W, Sher A, Litke AM, Mitra S, Chichilnisky EJ (2021)

Spatially patterned bi-electrode epiretinal stimulation for axon avoidance at cellular resolution. J Neural Eng 18:066007.

Virtanen P, et al. (2020) SciPy 1.0: fundamental algorithms for scientific computing in Python. Nat Methods 17:261–272.

Vrabec F (1966) The temporal raphe of the human retina. Am J Ophthalmol 62:926–938.

Walsh N, Ghosh KK, FitzGibbon T (2000) Intraretinal axon diameters of a New World primate, the marmoset (Callithrix jacchus). Clin Exp Ophthalmol 28:423–430.

Wandell BA (1995) Foundations of vision: behaviour, neuroscience, and computation. Sunderland, MA: Sinauer Associates.

Wang Z, Bovik AC, Sheikh HR, Simoncelli EP (2004) Image quality assessment: from error visibility to structural similarity. IEEE Trans Image Process 13:600–612.

Warland DK, Reinagel P, Meister M (1997) Decoding visual information from a population of retinal ganglion cells. J Neurophysiol 78:2336–2350.

Watanabe M, Rodieck RW (1989) Parasol and midget ganglion cells of the primate retina. J Comp Neurol 289:434–454.

Weiland JD, Cho AK, Humayun MS (2011) Retinal prostheses: current clinical results and future needs. Ophthalmology 118:2227–2237.

Weiland JD, Walston ST, Humayun MS (2016) Electrical stimulation of the retina to produce artificial vision. Annu Rev Vis Sci 2:273–294.

Wu EG, Sher A, Litke AM, Simoncelli EP, Chichilnisky EJ (2022) Maximum a posteriori natural scene reconstruction from retinal ganglion cells with deep denoiser priors. bioRxiv 492737. https://doi.org/10.1101/2022.05.19.492737.

Yu W-Q, Grzywacz NM, Lee E-J, Field GD (2017) Cell type-specific changes in retinal ganglion cell function induced by rod death and cone reorganization in rats. J Neurophysiol 118:434–454.

Zaidi M, Aggarwal G, Shah NP, Karniol-Tambour O, Goetz G, Madugula S, Gogliettino AR, Wu EG, Kling A, Brackbill N, Sher A, Litke AM, Chichilnisky EJ (2022) Inferring light responses of primate retinal ganglion cells using intrinsic electrical signatures. bioRxiv 493858. https://doi.org/10.1101/2022.05.29.493858.

Zhang Y, Jia S, Zheng Y, Yu Z, Tian Y, Ma S, Huang T, Liu JK (2020) Reconstruction of natural visual scenes from neural spikes with deep neural networks. Neural Netw 125:19–30.